Structural Safety 86 (2020) 101975

Contents lists available at ScienceDirect

Structural Safety

journal homepage: www.elsevier.com/locate/strusafe

Spectral identification of nonlinear multi-degree-of-freedom structural systems with fractional derivative terms based on incomplete non-stationary data

Ketson R.M. dos Santos, Olga Brudastova, Ioannis A. Kougioumtzoglou*

Department of Civil Engineering and Engineering Mechanics, Columbia University, 500 W 120th St, New York, NY 10027, United States

ARTICLE INFO

Keywords:
System identification
Nonlinear systems
Fractional derivative
Generalized harmonic wavelet
Incomplete data
Compressive sampling

ABSTRACT

A novel spectral identification technique is developed for determining the parameters of nonlinear and time-variant multi-degree-of-freedom (MDOF) structural systems based on available input-output (excitation-response) realizations. A significant advantage of the technique relates to the fact that it can readily account for the presence of fractional derivative terms in the system governing equations, as well as for the cases of non-stationary, incomplete and/or noise corrupted data. Specifically, the technique relies on recasting the governing equations as a set of multiple-input/multiple-output systems in the wavelet domain. Next, an l_1-norm minimization procedure based on compressive sampling theory is employed for determining the wavelet coefficients of the available incomplete non-stationary input-output data. Finally, these wavelet coefficients are utilized to reconstruct the non-stationary incomplete signals, and consequently, to determine system related time- and frequency-dependent wavelet-based frequency response functions and associated parameters. Two illustrative MDOF systems are considered in the numerical examples for demonstrating the reliability of technique. The first refers to a nonlinear time-variant system with fractional derivative terms, while the second addresses a nonlinear offshore structural system subjected to flow-induced forces. It is worth noting that for the offshore system, a novel recently proposed evolutionary version of the widely used JONSWAP spectrum is employed for modeling the non-stationary free-surface elevation in cases of time-dependent sea states.

1. Introduction

The development of robust system identification techniques is of paramount importance to methodologies for fault/damage detection, for monitoring of the structural system dynamic behavior, and for assessing its reliability. Although numerous and diverse system identification techniques have been proposed over the past few decades with varying degrees of success (see for instance the review papers and books [1–5]), there is still merit in developing novel and enhancing existing techniques considering the increasingly sophisticated modeling of structural systems. Indeed, a more realistic representation of engineering dynamical systems necessitates often the utilization of complex nonlinear relationships, the consideration of fractional calculus for more accurate (viscoelastic) material behavior modeling, as well as the mathematical treatment of excitations as (non-stationary) stochastic processes.

Specifically, the response of various structural and mechanical systems can be significantly nonlinear, and such behaviors typically become more prevalent as the system response amplitude increases (e.g., [6]). Indicative examples include nonlinear hysteretic behaviors of building structures due to severe earthquake excitations (e.g., [7–9]), and strong (non-smooth) nonlinearities exhibited by offshore systems subject to flow-induced forces (e.g., [10–12]). Further, the advanced mathematical tool of generalized calculus (referred to in the literature as fractional calculus) has been used recently in engineering mechanics for developing non-local continuum mechanics theories and for enhanced modeling of viscoelastic materials (e.g., [13–15]). Furthermore, in many real-life applications the measured available data may be not only non-stationary (and thus, special treatments are required based on joint time-frequency analysis tools such wavelets [16]), but also incomplete and/or corrupted (due to several reasons such as sensor failures and limited bandwidth/storage capacity [17]). Therefore, it is readily seen that robust system identification is required to address simultaneously a variety of challenges. In fact, most established system response analysis and identification techniques are tailored for treating conventional governing equations of motion, whereas accounting for

* Corresponding author.
E-mail address: ikougioum@columbia.edu (I.A. Kougioumtzoglou).

https://doi.org/10.1016/j.strusafe.2020.101975
Received 26 July 2019; Received in revised form 18 March 2020; Accepted 2 May 2020

generalized (fractional) derivative modeling poses significant challenges and is a topic of ongoing research (e.g., [18]). In general, various identification techniques have been developed in the literature for addressing cases of non-stationary data (e.g., [19,20]), for accounting for incomplete measured time-histories (e.g., [21,22]), or for treating systems with fractional derivative terms (e.g., [23–26]). Nevertheless, there are not many (if any) nonlinear system identification techniques that can address all three aforementioned challenges simultaneously in a consistent manner.

Recently, a nonlinear and time-variant single-degree-of-freedom (SDOF) oscillator parameter identification technique has been developed in [27]. The technique can be construed as a generalization of the multiple-input-single-ouput (MISO) methodology proposed by Bendat and co-workers (e.g., [28–30]) to account for non-stationary and incomplete data, as well as for fractional derivative modeling. In this paper, the technique is further extended to account for multi-degree-of-freedom (MDOF) systems. Two illustrative MDOF systems are considered in the numerical examples for demonstrating the reliability of technique, even in cases of noise corrupted and incomplete data. The first refers to a nonlinear time-variant system with fractional derivative terms, while the second addresses a nonlinear offshore structural system subjected to flow-induced forces. It is worth noting that for the offshore system, a novel recently proposed evolutionary version of the standard JONSWAP spectrum is employed for modeling the non-stationary free-surface elevation in cases of time-dependent sea states [31].

2. Addressing non-stationary and incomplete data

2.1. Non-stationary data: a harmonic wavelets approach

One of the main advantages of generalized harmonic wavelets (GHWs) [32] over alternative commonly used wavelet families (e.g., Morlet wavelets) relates to the fact that the time-frequency resolution achieved at each scale is essentially decoupled from the value of the central frequency. This is possible due to the utilization of two parameters (m, n) for defining the bandwidth at each scale. Thus, depending on the application, enhanced localized resolution in the frequency domain can be achieved where this is deemed appropriate. In passing, note that GHWs have found diverse applications in engineering dynamics including developing generalized joint time-frequency input-output (excitation-response) relationships (e.g., [33]), determining approximately the stochastic response of nonlinear systems (e.g., [34,35]), as well as identifying the time-variant parameters of structural systems based on measured available data (e.g., [36,27]). Next, some basic definitions and properties of harmonic wavelets are delineated for completeness. In particular, a wavelet of (m, n) scale and position k in time attains a representation in the frequency domain of the form

$$\Psi^{G}_{(m,n),k}(\omega) = \begin{cases} \frac{1}{(n-m)\Delta\omega}\exp\left(-i\frac{\omega k T_0}{n-m}\right), & m\Delta\omega \leq \omega < n\Delta\omega \\ 0, & \text{otherwise} \end{cases}, \tag{1}$$

where m, n and k are non-negative integers, and $\Delta\omega = \frac{2\pi}{T_0}$, where T_0 is the total duration of the signal, and $m\Delta\omega \leqslant \omega < n\Delta\omega$ is the bandwidth of the box-shaped spectrum. The inverse Fourier transform of Eq. (1) provides the time-domain representation

$$\Psi^{G}_{(m,n),k}(t) = \frac{\exp\left(in\Delta\omega\left(t-\frac{kT_0}{n-m}\right)\right) - \exp\left(im\Delta\omega\left(t-\frac{kT_0}{n-m}\right)\right)}{i\left(n-m\right)\Delta\omega\left(t-\frac{kT_0}{n-m}\right)}. \tag{2}$$

Further, the generalized harmonic wavelet transform (GHWT) of an arbitrary signal $x(t)$ is given by

$$W^{G}_{(m,n),k}[x] = \frac{n-m}{T_0}\int_{-\infty}^{\infty} x(t)\overline{\Psi^{G}_{(m,n),k}}(t)\mathrm{d}t, \tag{3}$$

and the inverse transform reconstructs exactly the target signal in the form

$$x(t) = \sum_{m,n}\sum_{k}\left(W^{G}_{(m,n),k}[x]\Psi^{G}_{(m,n),k}(t) + \overline{W^{G}_{(m,n),k}[x]\Psi^{G}_{(m,n),k}}(t)\right), \tag{4}$$

where the bar over an expression denotes complex conjugation. It has been shown recently that based on Parseval's theorem, on the theory of locally stationary processes (e.g., [37]), and accounting for the GHW non-overlapping box-shaped frequency spectrum, an estimate can be obtained for the underlying stochastic process evolutionary power spectrum (EPS) in the form (e.g., [38,34,39])

$$S_{xx}\left(\omega, t\right) = S^{xx}_{(m,n),k} = \frac{\mathbb{E}\left[|W^{G}_{(m,n),k}[x]|^2\right]}{(n-m)\Delta\omega}, \tag{5}$$

where $S_{xx}(\omega, t) = S^{xx}_{(m,n),k}$ is considered constant over the intervals $m\Delta\omega \leqslant \omega < n\Delta\omega$, and $\frac{kT_0}{n-m} \leqslant t < \frac{(k+1)T_0}{n-m}$. Note that the expectation operator in Eq. (5) implies that an ensemble of realizations compatible with the underlying non-stationary stochastic process is available. In a similar manner, the cross-EPS of two processes $x(t)$ and $y(t)$ can be estimated as

$$S_{xy}\left(\omega, t\right) = S^{xy}_{(m,n),k} = \frac{\mathbb{E}\left[W^{G}_{(m,n),k}[x]\overline{W^{G}_{(m,n),k}[y]}\right]}{(n-m)\Delta\omega}. \tag{6}$$

2.2. Incomplete data: a compressive sampling approach

During the past fifteen years, research efforts have focused on identifying and exploiting low-dimensional representations of high-dimensional data as well as on establishing conditions guaranteeing unique representation in the low-dimensional space. These theoretical results, coupled with potent convex optimization numerical algorithms, have triggered the birth of the currently expanding field of compressive sampling and have led to numerous impactful contributions in a wide range of application areas. Concisely, and focusing on signal processing under incomplete/missing data, compressive sampling allows for signal reconstruction even if the maximum frequency in the recorded signal is greater than half the signal's sampling rate. This is possible primarily due to the assumptions of sparsity and incoherence. In other words, the signal is considered sparse in some known basis, while at the same time has a non-sparse representation in the sampling domain. Also, the restricted isometry property is required for efficient signal reconstruction; see the pioneering work in [40–42], and the book in [43] for more details.

Compressive sampling is typically employed for determining the sparsest signal representation in a given basis subject to available data. Specifically, given a sample record $\mathbf{y} \in \mathbb{R}^{N_0-N_m}$, where N_0 is the original sample length, and N_m is the number of missing data points, and considering the locations of the missing data to be known, the corresponding sampling matrix $\mathbf{B} \in \mathbb{R}^{(N_0-N_m)\times N_0}$ can be defined as

$$\mathbf{y} = \mathbf{B}\mathbf{x}, \tag{7}$$

where $\mathbf{x} \in \mathbb{R}^{N_0}$ is the coefficients vector of the selected basis assumed to be sparse. Clearly, Eq. (7) represents an underdetermined system of equations with infinite solutions given that $N_0 - N_m < N_0$. The sparsest solution can be determined (at least theoretically) by applying an l_0-norm minimization approach. However, this yields a non-convex optimization problem, which is most often computationally intractable. Instead, the l_1-norm can be minimized, which also promotes sparsity and in many cases yields results comparable to applying an l_0-norm approach. Most importantly, employing an l_1-norm minimization solution framework leads to a convex optimization problem of the form

$$\min\|\mathbf{x}\|_{l_1} \text{ subject to } \mathbf{y} = \mathbf{B}\mathbf{x}, \tag{8}$$

which can be solved via, for instance, basis pursuit [44] or greedy algorithms [45]. In passing, note that there exist various other currently emerging tools and techniques for enhancing solution sparsity and for exploiting additional information in the data. These include alternative to l_1-norm minimization formulations and iterative re-weighting solution schemes, Bayesian approaches, as well as structured sparsity and dictionary learning strategies (e.g., [46–48]).

Compressive sampling has found a variety of applications in structural dynamics over the past few years, especially related to efficient data compression and storage at the sensors level and to fast data transmission. This has proved quite advantageous for real-time structural health monitoring, not only from a cost efficiency perspective, but also in cases of reconstructing corrupted signals; see for instance [49–55,22] for some indicative references.

Further, compressive sampling based techniques have also been developed within the context of random processes to address problems in stochastic engineering dynamics related to spectral analysis and estimation under vastly incomplete data. Specifically, Kougioumtzoglou and co-workers relied on compressive sampling theory for stationary and non-stationary stochastic process power spectrum estimation subject to missing data [56]. This was done in conjunction with an l_1-norm optimization algorithm for obtaining a sparse representation of the signal in the selected basis (Fourier/ wavelets). The technique has been enhanced by utilizing an adaptive basis re-weighting scheme and/or an l_p-norm ($0 < p < 1$) optimization algorithm for increasing further the sparseness of the solution (e.g., [57]). The above developments have found recently diverse applications in marine engineering. Indicatively, a methodology based on compressive sampling has been proposed for efficient processing and joint time-frequency analysis of relatively long water wave records by enabling reconstruction of data recorded at a very low sampling rate (sub-Nyquist) [58]. Further, a compressive sampling technique has been developed in [59] for extrapolating in the spatial domain and estimating the space-time characteristics of a sea state based on data collected at very few spatially sparse points (e.g., wave buoys). This is of considerable importance to a number of marine engineering applications involving three-dimensional waves interacting with marine structures, such as optimizing arrays of wave energy converters.

For the non-stationary processes considered herein, the EPS is estimated by Eq. (5) based on an ensemble of time-histories, whereas an appropriately modified GHW basis is utilized for the case of missing data; see also [56] for a more detailed presentation on compressive sampling based EPS estimation under incomplete data.

3. Identification technique

3.1. GHW-based excitation-response relationships for linear time-variant MDOF systems with fractional derivative terms

In this section, a GHW-based input-output (excitation-response) relationship for MDOF structural systems is derived, which is of paramount importance to the development of the identification technique in Section 3.2. Specifically, the celebrated spectral input-output relationship of random vibration theory, which is valid for stationary processes (e.g., [6]), is generalized to account for non-stationary processes with arbitrary EPS forms. Thus, a joint time-frequency response analysis is possible. It is noted that the analysis and derivations in this section are based on a local stationarity assumption. In particular, it can be argued that for relatively stiff and heavily damped systems the related impulse response function is short-lived, and thus, local stationarity can be justified. Nevertheless, it has been shown recently that an enhanced GHW-based input-output relationship valid for SDOF oscillators with integer order derivatives can circumvent the above restriction [33]. Its generalization to account for MDOF systems and for fractional derivative terms is identified as a topic for future work.

Consider a MDOF linear time-variant (LTV) system with fractional derivative elements, whose motion is governed by

$$\mathbf{M}(t)\ddot{\mathbf{x}} + \mathbf{C}(t)\mathrm{D}^q[\mathbf{x}(t)] + \mathbf{K}(t)\mathbf{x} = \mathbf{f}(t), \tag{9}$$

where $\mathbf{x}(t)$ is the oscillator response displacement; $\mathbf{M}(t)$, $\mathbf{C}(t)$, and $\mathbf{K}(t)$ are the time-varying mass, damping, and stiffness matrices, respectively; $\mathbf{f}(t)$ is a realization compatible with a Gaussian, zero-mean non-stationary stochastic excitation vector process with an EPS $S_{\mathbf{f}}(\omega, t)$; and $\mathrm{D}^q[\cdot]$ denotes Caputo's fractional derivative [60] defined as

$$\mathrm{D}^q\left[\mathbf{x}(t)\right] = \frac{1}{\Gamma(1-q)}\int_0^t \frac{\dot{\mathbf{x}}(\tau)}{(t-\tau)^q}\mathrm{d}\tau, \tag{10}$$

where $0 \leqslant q < 1$; and $\Gamma(z)$ is the gamma function. Note, in passing, that alternative fractional derivative definitions, such as the Riemann-Liouville and the Grunwald-Letnikov, exist in the literature (e.g., [60]).

Next, applying the GHWT of Eq. (4) to Eq. (9) and assuming that the mass, stiffness, and damping elements are slowly varying functions in time, and thus, approximately constant over the compact support of the GHW in the time domain (i.e., $\mathbf{M}(t) \approx \mathbf{M}_k$, $\mathbf{K}(t) \approx \mathbf{K}_k$, and $\mathbf{C}(t) \approx \mathbf{C}_k$), yields

$$\mathbf{M}_k W^G_{(m,n),k}[\ddot{\mathbf{x}}] + \mathbf{C}_k W^G_{(m,n),k}[\mathrm{D}^q[\mathbf{x}(t)]] + \mathbf{K}_k W^G_{(m,n),k}[\mathbf{x}] = W^G_{(m,n),k}[\mathbf{f}]. \tag{11}$$

In the following, relationships between the GHWT of derivatives of x and the GHWT of x are sought for to further manipulate Eq. (11). In this regard, it is rather straightforward to generalize the relationships (referring to scalar functions) developed in [35] to account for vector-valued functions. Specifically, following closely [35], relying on the time localization of the GHW, on the linearity property of the fractional derivative, and assuming that the frequency band $[m\Delta\omega,\ n\Delta\omega]$ is relatively small and defining $\omega_{c,(m,n),k} = \frac{(n+m)}{2}\Delta\omega$, yields the approximate expressions

$$W^G_{(m,n),k}[\dot{\mathbf{x}}] = i\omega_{c,(m,n),k} W^G_{(m,n),k}[\mathbf{x}], \tag{12}$$

$$W^G_{(m,n),k}[\ddot{\mathbf{x}}] = -\omega^2_{c,(m,n),k} W^G_{(m,n),k}[\mathbf{x}], \tag{13}$$

$$W^G_{(m,n),k}[\mathrm{D}^q[\mathbf{x}(t)]] = (i\omega_{c,(m,n),k})^q W^G_{(m,n),k}[\mathbf{x}]. \tag{14}$$

Substituting Eqs. (12)–(14) into Eq. (11) leads to the input-output relationship

$$W^G_{(m,n),k}[\mathbf{x}](-\omega^2_{c,(m,n),k}\mathbf{M}_k + (i\omega_{c,(m,n),k})^q\mathbf{C}_k + \mathbf{K}_k) = W^G_{(m,n),k}[\mathbf{f}]. \tag{15}$$

Next, applying complex conjugation to Eq. (15), taking the expectation operator and considering Eqs. 5,6 yields

$$\mathbf{S}^{\mathbf{x}}_{(m,n),k} = \mathbf{H}^G_{(m,n),k}\mathbf{S}^{\mathbf{f}}_{(m,n),k}\overline{\mathbf{H}^G_{(m,n),k}}^T. \tag{16}$$

Note that $\mathbf{H}^G_{(m,n),k}$ in Eq. (16) denotes the GHW frequency response function (GHW-FRF) given by

$$\mathbf{H}^G_{(m,n),k} = (-\omega^2_{c,(m,n),k}\mathbf{M}_k + (i\omega_{c,(m,n),k})^q\mathbf{C}_k + \mathbf{K}_k)^{-1}. \tag{17}$$

Clearly, Eq. (17) represents a time- and frequency-dependent GHW-FRF, while Eq. (16) can be construed as a generalization of the celebrated Wiener-Khinchin spectral input-output relationship of the stationary linear random vibration theory [6]. As noted earlier, local stationarity has been assumed for the derivation of Eq. (17), whereas future work towards weakening this assumption relates to generalizing the relationships developed in [33] to account for fractional derivative operators and vector-valued functions; see also [33,35] for more details.

3.2. Multiple-input/single-output (MISO) identification technique

In this section, a novel MISO system parameter identification technique is developed by relying on and generalizing pioneering work

by Bendat and co-workers [28–30]. The original development of the MISO technique, valid for stationary processes, has found a wide range of applications in parameter identification of diverse engineering systems (e.g., [61–64]). The technique has been generalized in [36] to account for non-stationary excitation-response data and for time-varying system parameters, while it has been extended recently in [27] to address systems endowed with fractional derivative elements and subject to incomplete measured data. Nevertheless, the previous developments in [36] and in [27] refer to SDOF oscillators. In this regard, the present work generalizes further the MISO technique to account for MDOF systems subject to incomplete non-stationary data, even when endowed with fractional derivative elements.

It is noted that the developed generalization in this paper is not trivial and exhibits considerable methodological novelty. Specifically, first, the derivation of appropriate excitation-response relationships for MDOF systems in the GHW domain is a requirement for the development of the identification technique. In this regard, the herein derived GHW-based input-output relationships for MDOF systems with fractional derivatives terms (see Section 3.1) are presented for the first time in the literature. Second, the identification technique developed in the following is considerably different to the one in [27], which corresponds to SDOF systems. In fact, in comparison to the technique in [27] where the SDOF oscillator is cast directly into a MISO system in the wavelet domain, an additional step is required in the herein proposed formulation; that is, the MDOF system is cast, first, into a multiple-input/multiple-output (MIMO) system in the wavelet domain with correlated inputs, and subsequently, this MIMO system is cast into a set of MISO systems. This fundamental difference complicates significantly the ensuing analysis as the decorrelation procedure and resulting equations become more complex as compared to the ones in [27]. Overall, it can be readily seen that various non-trivial challenges are addressed in the following for generalizing the identification technique from SDOF to MDOF systems.

Consider a general MIMO system, where the GHWT is applied to the l input and the $r+1$ different output time-histories as shown in Fig. 1, where $\mathbf{H}^{G}_{(m,n),k}$ accounts for an arbitrary time- and frequency-dependent GHW-FRF (see Eq. 16). Next, accounting for correlations between the various output records, the original MIMO system can be equivalently cast as a set of MISO systems, with each MISO system corresponding to a specific output and to $l+r$ (possibly correlated) inputs; see Fig. 2, and [65,30] for more details. Further, to address the possible correlations between the inputs, a decorrelation scheme based on conditioned spectra, presented in [30] (see also [66]) and extended herein to account for time- and frequency-dependent EPS, is outlined next. In particular, taking into account the i-th input x_i and the output f , and based on Eqs. 5,6, consider the GHW-based auto-spectra $S^{ii}_{(m,n),k} = S^{x_i x_i}_{(m,n),k}$, $S^{ff}_{(m,n),k}$, and cross-spectra $S^{ij}_{(m,n),k} = S^{x_i x_j}_{(m,n),k}$, $S^{if}_{(m,n),k} = S^{x_i f}_{(m,n),k}$, where $i, j = 1, 2, \ldots, l+r$. The conditioned EPS are then given by

$$S^{ij,c}_{(m,n),k} = S^{ij.(i-1)!}_{(m,n),k}, \tag{18}$$

$$S^{if,c}_{(m,n),k} = S^{if.(i-1)!}_{(m,n),k}, \tag{19}$$

where

$$S^{ij.r!}_{(m,n),k} = S^{ij.(r-1)!}_{(m,n),k} - \frac{S^{rj.(r-1)!}_{(m,n),k}}{S^{rr.(r-1)!}_{(m,n),k}} S^{ir.(r-1)!}_{(m,n),k}, \quad r < i, \tag{20}$$

$$S^{if.r!}_{(m,n),k} = S^{if.(r-1)!}_{(m,n),k} - \frac{S^{rf.(r-1)!}_{(m,n),k}}{S^{rr.(r-1)!}_{(m,n),k}} S^{ir.(r-1)!}_{(m,n),k}, \quad r < i. \tag{21}$$

Note that for $r = 0$, $S^{ij.r!}_{(m,n),k} = S^{ij}_{(m,n),k}$ and $S^{if.r!}_{(m,n),k} = S^{if}_{(m,n),k}$. Next, utilizing the conditioned GHW-based EPS, the linear operators $L^{G}_{iy,(m,n),k}$ are defined that relate the uncorrelated input records $y_i(t)$ to a specific output $f(t)$ via the equation (see also Fig. 3)

$$\mathbf{L}^{G}_{if,(m,n),k} = \frac{S^{if,c}_{(m,n),k}}{S^{ii,c}_{(m,n),k}}. \tag{22}$$

The output auto-EPS $S^{ff}_{(m,n),k}$ can then be evaluated as (see also [65,67,36])

$$S^{ff}_{(m,n),k} = \sum_{i=1}^{l+r} |\mathbf{L}^{G}_{if,(m,n),k}|^2 S^{ii,c}_{(m,n),k}. \tag{23}$$

In this regard, GHW-based generalized versions of coherence functions between each of the inputs $y_i(t)$ and the output $f(t)$ are given by

$$(\gamma^{if}_{(m,n),k})^2 = \frac{|S^{if,c}_{(m,n),k}|^2}{S^{ii,c}_{(m,n),k} S^{ff,c}_{(m,n),k}}, \quad i = 1, 2, \ldots, l+r. \tag{24}$$

while the GHW-based cumulative coherence function (GHW-CCF) is defined as

$$(\gamma^{f:z}_{(m,n),k})^2 = \sum_{i=1}^{l+r} (\gamma^{if}_{(m,n),k})^2. \tag{25}$$

The GHW-CCF in Eq. (25) is used as an indicator of the modeling error providing information about the "goodness-of-fit" of the model subject to the measured data (e.g., [36]). Note that its value should approach unity in cases where the model provides a good fit. The interested reader is also directed to [30,36] for more details on the topic.

Focusing next on structural systems whose governing equation of motion can be cast in the form of a MIMO system shown in Fig. 1, consider a nonlinear version of the MDOF system of Eq. (9), given by

$$\mathbf{M}(t)\ddot{\mathbf{x}} + \mathbf{C}(t)\mathrm{D}^{q}[\mathbf{x}(t)] + \mathbf{K}(t)\mathbf{x} + \mathbf{g}(\mathbf{x}, \dot{\mathbf{x}}) = \mathbf{f}(t), \tag{26}$$

where $\mathbf{g}(\mathbf{x}, \dot{\mathbf{x}})$ is an arbitrary nonlinear vector function of the response displacement and velocity. Next, it is assumed that $\mathbf{g}(\mathbf{x}, \dot{\mathbf{x}})$ can be represented by a superposition of zero-memory nonlinear transformations and linear sub-systems (e.g., [68]) in the form

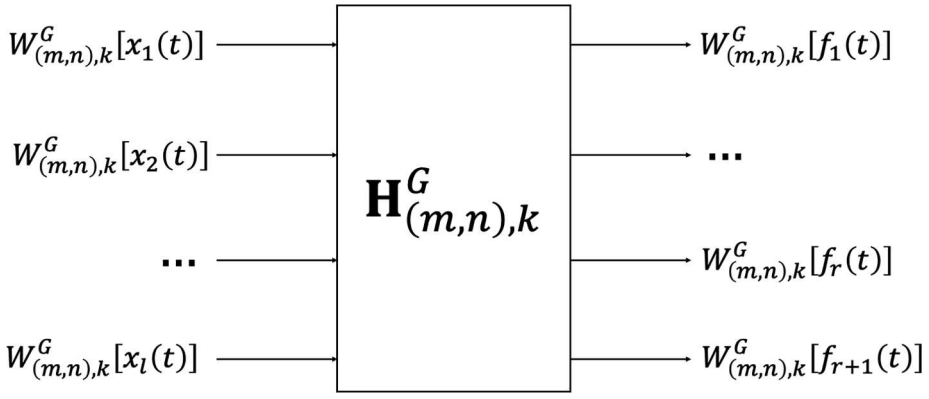

Fig. 1. MIMO model with l inputs and $r+1$ outputs.

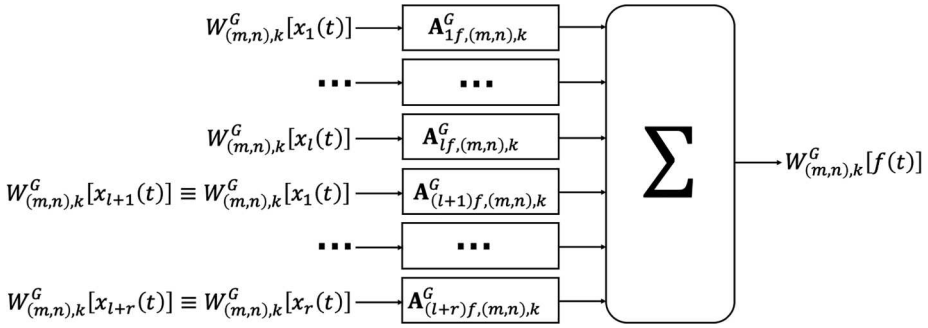

Fig. 2. MISO model with $l + r$ potentially correlated inputs and a specific output.

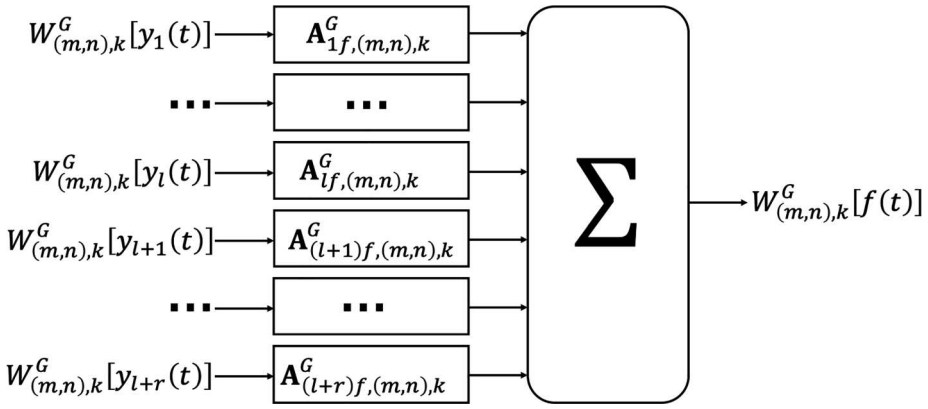

Fig. 3. MISO model with $l + r$ uncorrelated inputs.

$$\mathbf{g}(\mathbf{x}, \dot{\mathbf{x}}) = \sum_{i=1}^{M} \mathbf{A}_i \frac{\mathrm{d}}{\mathrm{d}t}\mathbf{p}_i(\mathbf{x}). \tag{27}$$

In Eq. (27), $\mathbf{A}_i$ are matrices with functions as entries to be defined in the following, $\mathbf{p}_i$ are zero-memory nonlinear transformations; and M is the total number of base functions in the representation of $\mathbf{g}(\mathbf{x}, \dot{\mathbf{x}})$. Substituting Eq. (27) into Eq. (26) leads to

$$\mathbf{M}(t)\ddot{\mathbf{x}} + \mathbf{C}(t)\mathrm{D}^q\left[\mathbf{x}(t)\right] + \mathbf{K}(t)\mathbf{x} + \sum_{i=1}^{M} \mathbf{A}_i \frac{\mathrm{d}}{\mathrm{d}t}\mathbf{p}_i(\mathbf{x}) = \mathbf{f}(t). \tag{28}$$

Taking the GHWT of Eq. (28) yields (see also [27])

$$\sum_{i=1}^{M+1} \mathbf{A}^G_{i,(m,n),k} W^G_{(m,n),k}[\mathbf{x}_i] + W^G_{(m,n),k}[\mathbf{z}] = W^G_{(m,n),k}[\mathbf{f}], \tag{29}$$

where $\mathbf{A}^G_{i,(m,n),k}$ are unknown time- and frequency-dependent GHW-FRFs, and $\mathbf{z}(t)$ accounts for added extraneous noise. Note that the inputs x_i relate to x and $p_i(x)$ (system reponses), whereas the outputs $\mathbf{f}(t)$ relate to the system excitation. Further, due to its vector-valued character, each term $W^G_{(m,n),k}[\mathbf{x}_i]$ corresponds to n inputs, where n is the number of degrees of freedom of the structural system. Thus, the total number of inputs is equal to $n(M + 1)$. Comparing Eq. (29) with Eq. (15), it can be readily seen that

$$\mathbf{A}^G_{1,(m,n),k} = [\mathbf{H}^G_{(m,n),k}]^{-1} = -\omega^2_{c,(m,n),k}\mathbf{M}_k + (i\omega_{c,(m,n),k})^q\mathbf{C}_k + \mathbf{K}_k. \tag{30}$$

However, $W^G_{(m,n),k}[\mathbf{x}_i]$ represent, in general, mutually correlated inputs. Thus, by employing the decorrelation scheme described in Eqs. (18)–(23) (see also [66,67,30,36]) the GHW-FRFs are given by

$$\mathbf{A}^G_{i,(m,n),k} = \mathbf{L}^G_{if,(m,n),k} - \sum_{j=i+1}^{M+N} \mathbf{A}^G_{j,(m,n),k} \frac{S^{ij,c}_{(m,n),k}}{S^{ii,c}_{(m,n),k}}, \tag{31}$$

where $i = 1, \ldots, M+N$, N is the number of degrees of freedom of the system, and $\mathbf{A}^G_{i,(m,n),k}$ is computed for the different outputs of the MISO system ($\mathbf{f}$).

3.3. Mechanization of the technique

The herein developed parameter identification technique is summarized in the following. In the ensuing analysis, it is assumed that the mass matrix $\mathbf{M}(t)$ is known, whereas the unknowns are, in general, the matrices $\mathbf{C}(t)$, $\mathbf{K}(t)$, the fractional derivative order q, as well as nonlinearity parameters related to function $\mathbf{g}(\mathbf{x}, \dot{\mathbf{x}})$.

1. Provided records of excitation-response time histories, apply Eqs. 5,6 and estimate the auto- and cross-EPS $S^{x_ix_i}_{(m,n),k}$, $S^{f_if_i}_{(m,n),k}$, $S^{x_ix_j}_{(m,n),k}$, $S^{f_if_j}_{(m,n),k}$, $S^{x_if_j}_{(m,n),k}$ for all input and output processes. In case of incomplete/missing data, apply Eqs. 5,6 in conjunction with the compressive sampling technique delineated in Section 2.2.
2. Evaluate the GHW-CCF $(\gamma^{f:x}_{(m,n),k})^2$ via Eq. (25) and select appropriate frequency ranges to identify the system parameters.
3. Estimate the GHW-FRFs $\mathbf{A}^G_{i,(m,n),k}$ via Eq. (31).
4. Determine the unknown system parameters. Specifically, $\mathbf{K}_k$ is determined from $\mathbf{A}^G_{1,(m,n),k}$ for $\omega_{c,(m,n),k} = 0$. Further, casting $\mathbf{A}^G_{1,(m,n),k}$, equivalently, in the form

$$\mathbf{A}^G_{1,(m,n),k} = \left[\omega^2_{c,(m,n),k}\mathbf{M}_k + \mathbf{K}_k + \omega^q_{c,(m,n),k}\cos\left(q\frac{\pi}{2}\right)\mathbf{C}_k\right] + i\left[\omega^q_{c,(m,n),k}\sin\left(q\frac{\pi}{2}\right)\mathbf{C}_k\right], \tag{32}$$

and manipulating, yields an estimate for the fractional derivative order in the form

$$q = \frac{2}{\pi}\mathrm{atan}\left[\frac{\mathrm{Im}(\mathbf{A}^G_{1,(m,n),k})}{\mathrm{Re}(\mathbf{A}^G_{1,(m,n),k}) - \mathbf{K}_k - \omega^2_{c,(m,n),k}\mathbf{M}_k}\right]. \tag{33}$$

Next, considering the imaginary part of Eq. (32), the damping matrix is obtained as

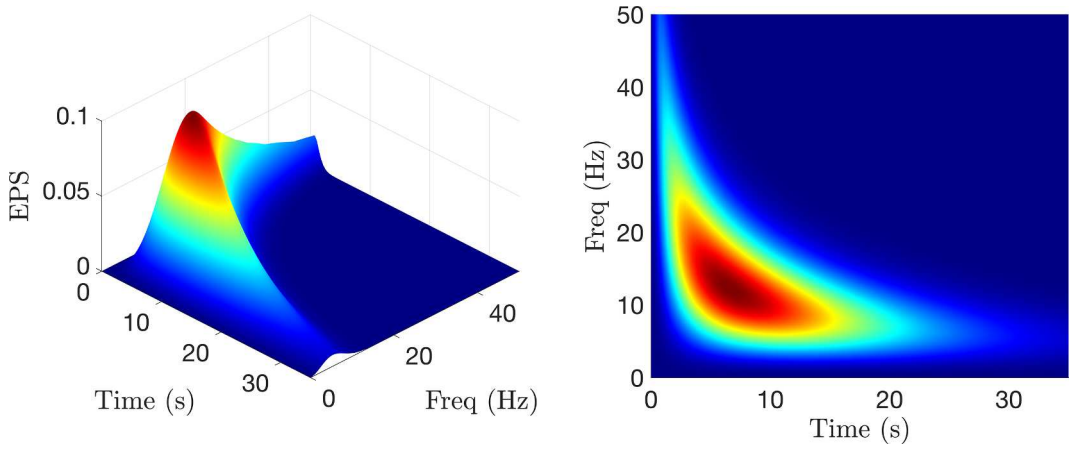

Fig. 4. Non-separable evolutionary excitation power spectrum.

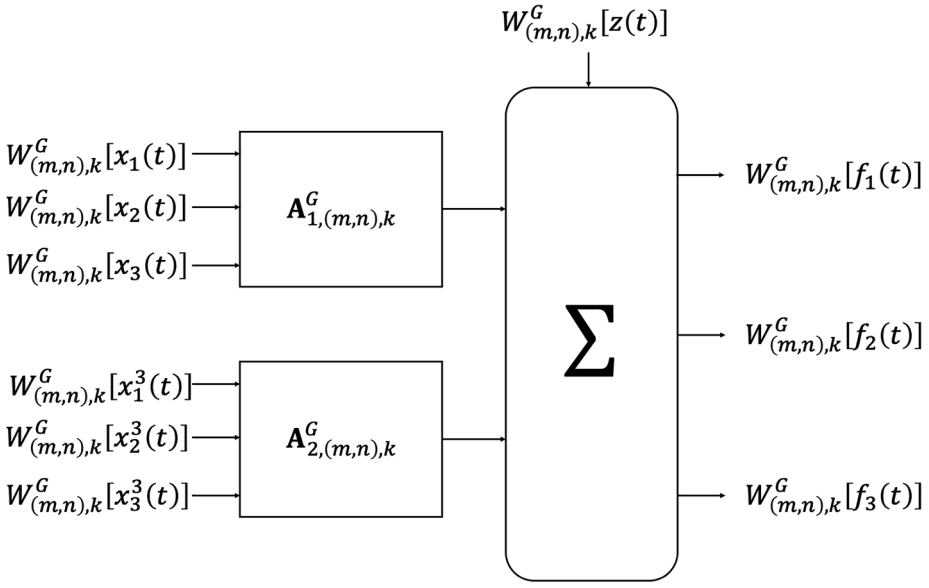

Fig. 5. 3-DOF Duffing oscillator recast as a MIMO problem.

$$\mathbf{C}_k = \frac{\mathrm{Im}[\mathbf{A}^G_{1,(m,n),k}]}{\omega^q_{c,(m,n),k}\sin\left(q\frac{\pi}{2}\right)}. \tag{34}$$

Finally, based on further consideration of the specific form of the nonlinear function $\mathbf{g}(\mathbf{x}, \dot{\mathbf{x}})$ and the related GHW-FRFs $\mathbf{A}^G_{i,(m,n),k}$, $i = 2, \ldots, M+1$, associated nonlinearity parameters can be obtained; see Section 4 for indicative numerical examples.

It is noted that in the above presented configuration, "excitation" and "response" have the standard roles of "input" and "output" in the MIMO system modeling, while the structural system parameters are considered to be the "unknowns" to be identified. Clearly, these roles can be altered based on the type of measured data available and the identification objective. In this regard, Eq. (28) can be readily re-arranged so that the herein developed MISO identification approach is still applicable in a straightforward manner.

4. Numerical examples

To demonstrate the accuracy and reliability of the herein developed system parameter identification technique, two indicative systems are considered in this section whose dynamics is governed by Eq. (24). The first refers to a 3-DOF time-variant Duffing oscillator with fractional derivative elements, while the second relates to a 2-DOF nonlinear time-variant structural system subject to flow-induced forces. In the former case, the oscillator parameters are considered to be the unknowns according to Section 3.3, whereas in the latter case the unknowns are the time-varying drag and inertia coefficients.

Further, the excitation is modeled as a non-stationary stochastic vector process with an EPS $\mathbf{S}(\omega, t)$. In this regard, time-histories compatible with the excitation EPS are generated by employing the spectral representation technique (e.g., [69,70]); that is,

$$f_i(t) = 2\sum_{j=0}^{s-1}\sqrt{S_{f_i}(j\Delta\omega, t)\Delta\omega}\cos(j\Delta\omega t + \phi_j), \tag{35}$$

where s refers to the discretization in the frequency domain, $\Delta\omega$ corresponds to the frequency increment, and ϕ_j are independent random phases uniformly distributed over the interval $[0, 2\pi]$. To integrate numerically Eq. (26) and determine response realizations, the standard L1-algorithm [71], which utilizes a discretization of the fractional derivative, is employed.

The robustness of the technique in the presence of both corrupted and incomplete data is assessed by considering two distinct cases: (a) complete excitation-response time histories, and (b) incomplete excitation-response time histories with added noise. Herein, various percentages of missing data (i.e., 5%, 10%, and 20%) are considered in

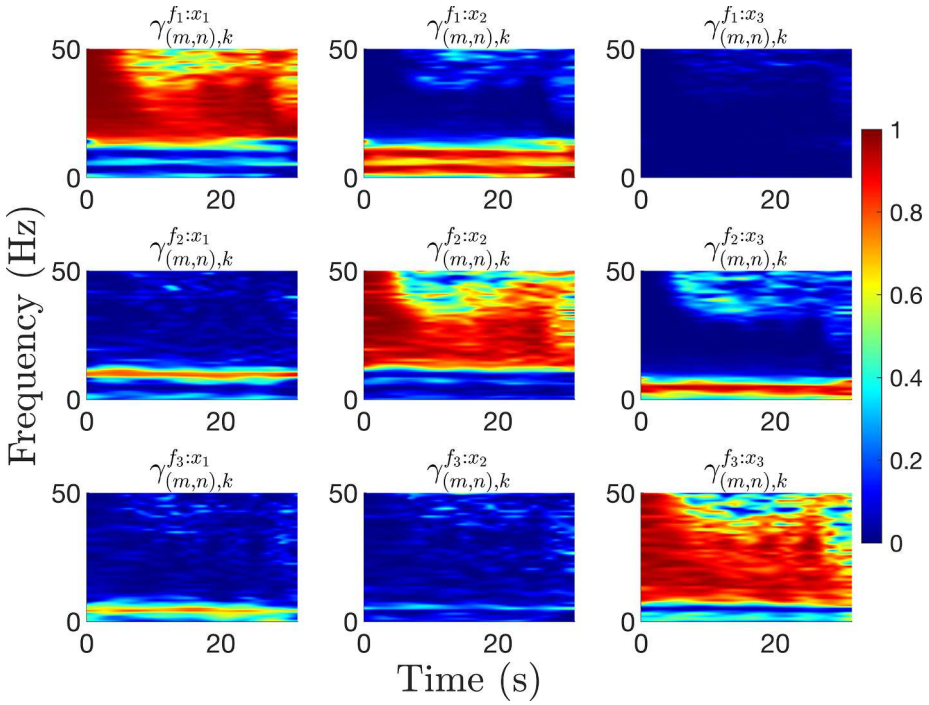

Fig. 6. Estimated GHW-CCF (complete time histories) for a 3-DOF Duffing time-variant oscillator with fractional derivative terms ($q = 0.5$, $\varepsilon_1 = 15$, $\varepsilon_2 = 10$ and $\varepsilon_3 = 5$).

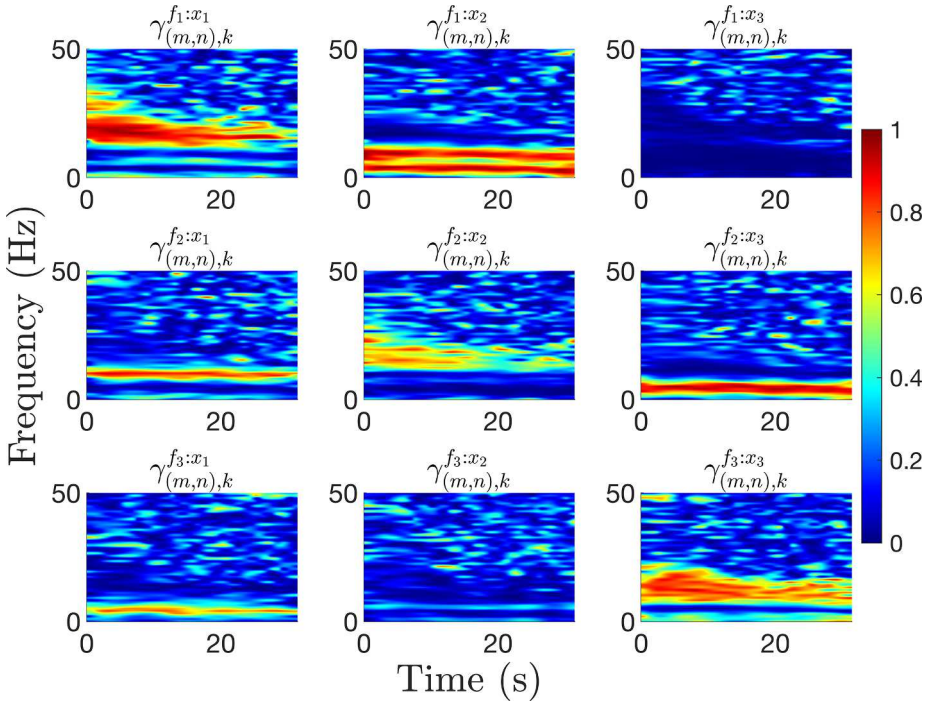

Fig. 7. Estimated GHW-CCF (incomplete time histories – 20% missing data - corrupted with noise) for a 3-DOF Duffing time-variant oscillator with fractional derivative terms ($q = 0.5$, $\varepsilon_1 = 15$, $\varepsilon_2 = 10$ and $\varepsilon_3 = 5$).

uniformly distributed random locations in the signals. The added noise is modeled as a Gaussian white noise vector process with a signal-to-noise ratio (SNR) of 40 dB; i.e. the standard deviation of the white noise is equivalent to 10 percent of the standard deviation of the signal. Furthermore, the following two metrics are employed for quantifying the error between the estimated and target parameters, i.e.,

$$\text{Error}_1 = \text{E}\left[\frac{\textit{identified-target}}{\textit{target}}\right], \tag{36}$$

and

$$\text{Error}_2 = \text{E}\left[\frac{|\textit{identified-target}|}{\textit{target}}\right], \tag{37}$$

where $\text{E}[\cdot]$ denotes the averaging operator over the time domain, and $|\cdot|$

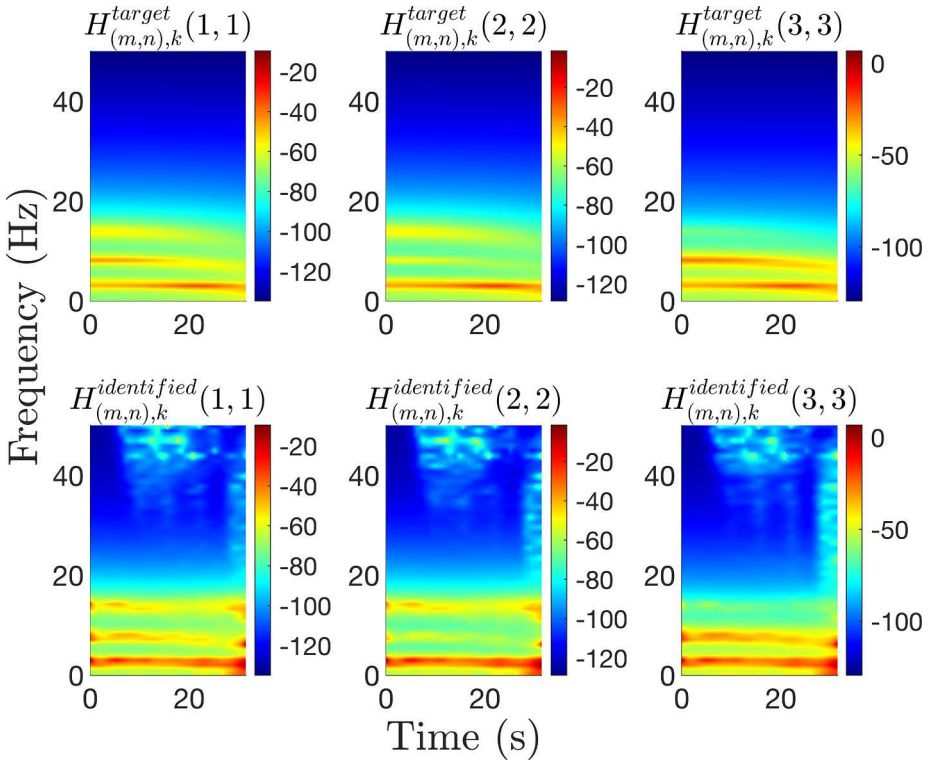

Fig. 8. Comparison between the target and the estimated GHW-FRF (complete time histories) for a 3-DOF Duffing time-variant oscillator with fractional derivative terms ($q = 0.5$, $\varepsilon_1 = 15$, $\varepsilon_2 = 10$ and $\varepsilon_3 = 5$).

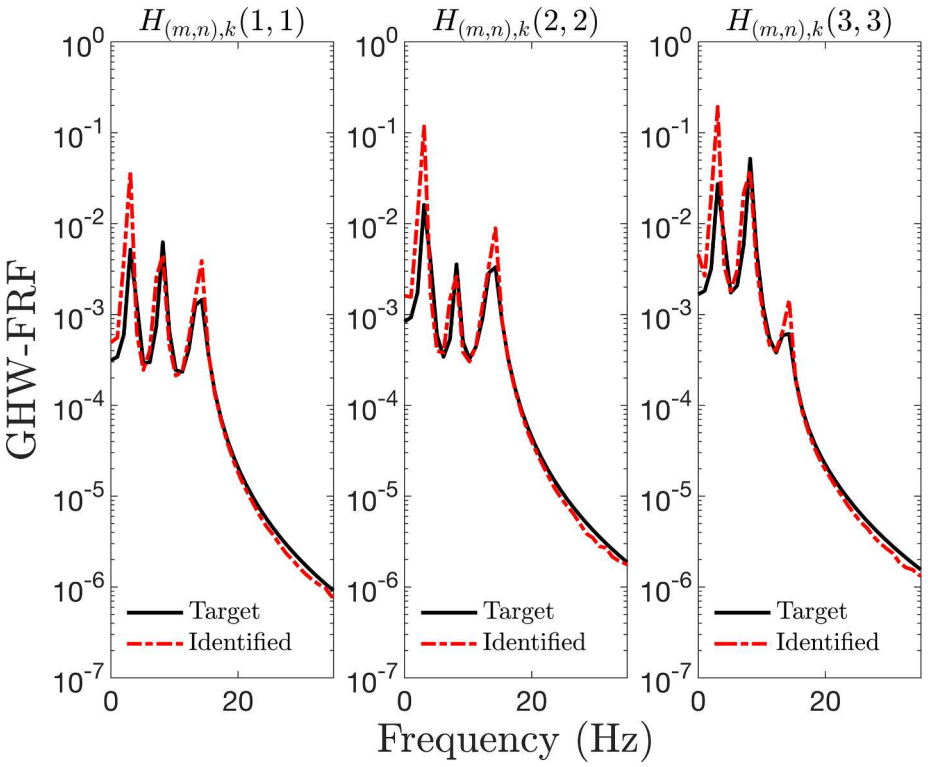

Fig. 9. Comparison between the target and the estimated GHW-FRF (complete time histories) at $t = 6.2s$ for a 3-DOF Duffing time-variant oscillator with fractional derivative terms ($q = 0.5$, $\varepsilon_1 = 15$, $\varepsilon_2 = 10$ and $\varepsilon_3 = 5$).

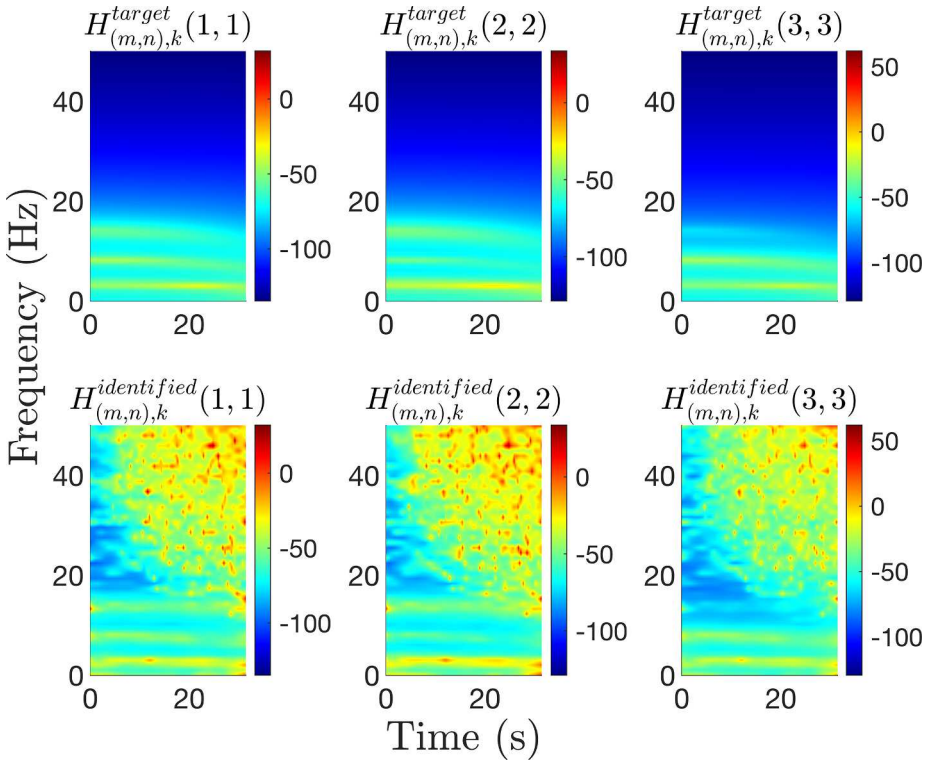

Fig. 10. Comparison between the target and the estimated GHW-FRF (incomplete time histories – 20% missing data - corrupted with noise) for a 3-DOF Duffing time-variant oscillator with fractional derivative terms ($q = 0.5$, $\varepsilon_1 = 15$, $\varepsilon_2 = 10$ and $\varepsilon_3 = 5$).

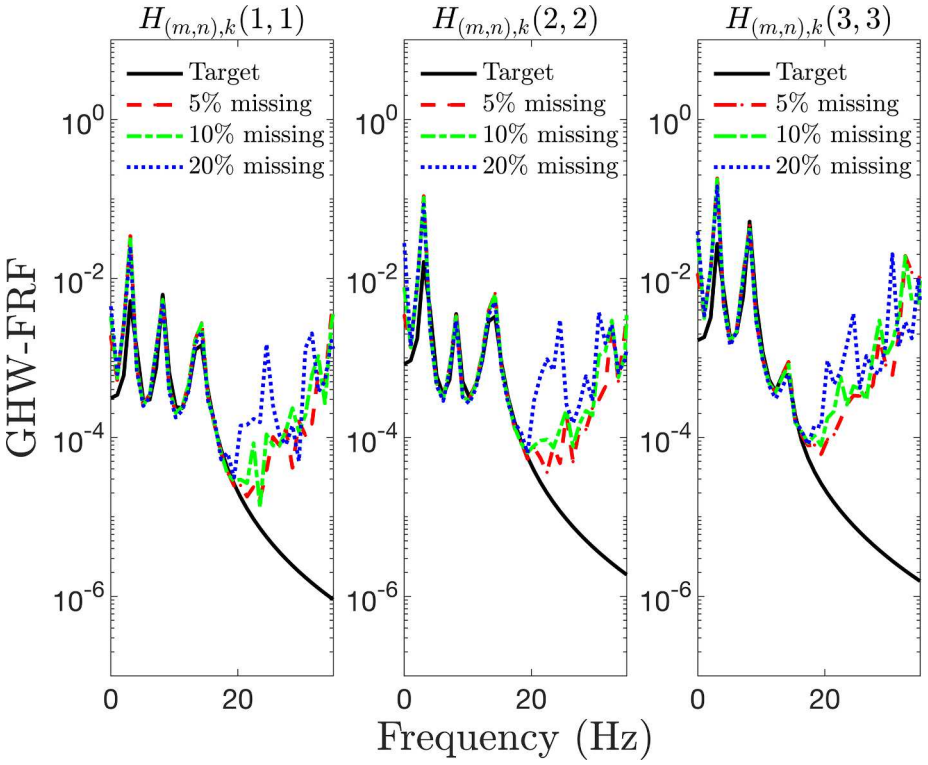

Fig. 11. Comparison between the target and the estimated GHW-FRF (incomplete time histories – 5%, 10% and 20% missing data - corrupted with noise) for a 3-DOF Duffing time-variant oscillator with fractional derivative terms ($q = 0.5$, $\varepsilon_1 = 15$, $\varepsilon_2 = 10$ and $\varepsilon_3 = 5$).

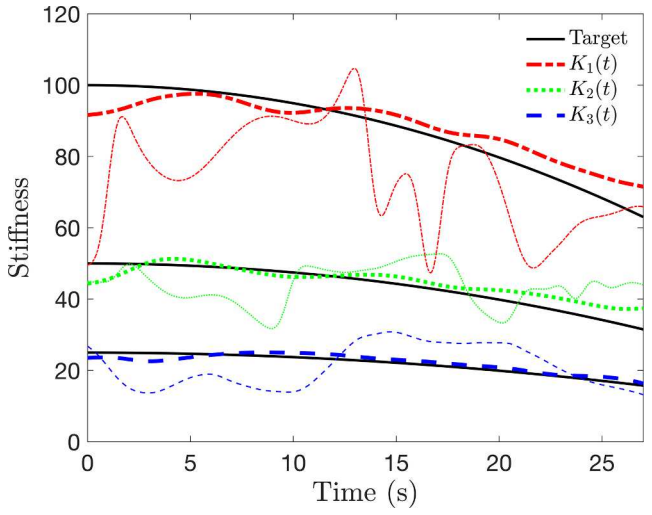

Fig. 12. Comparison between the target and the estimated stiffness elements for a 3-DOF Duffing oscillator with fractional derivative terms ($q = 0.5$, $\varepsilon_1 = 15$, $\varepsilon_2 = 10$ and $\varepsilon_3 = 5$) considering complete time histories (thick curves) and incomplete time histories - 20% missing data - corrupted with noise (thin curves).

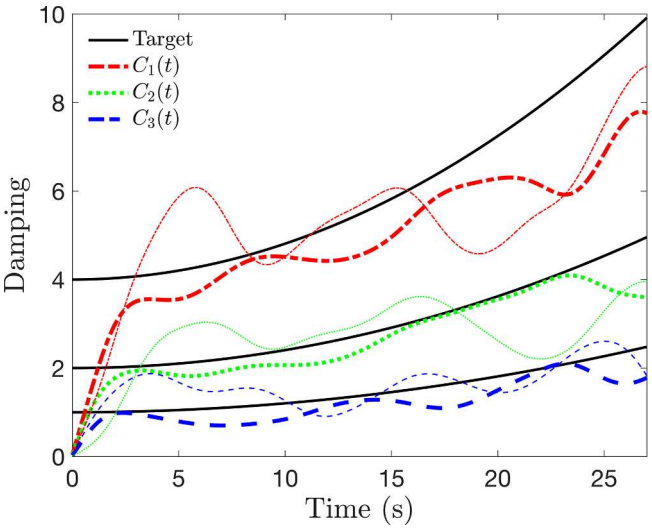

Fig. 13. Comparison between the target and the estimated damping elements for a 3-DOF Duffing oscillator with fractional derivative terms ($q = 0.5$, $\varepsilon_1 = 15$, $\varepsilon_2 = 10$ and $\varepsilon_3 = 5$) considering complete time histories (thick curves) and incomplete time histories - 20% missing data - corrupted with noise (thin curves).

Table 2
Identified nonlinearity parameters and fractional derivative order.

Parameter	Target	Complete	Missing (20%)/Noise	Missing (10%)/Noise	Missing(5%)/ Noise
ε_1	15	14.264	13.173	15.618	14.252
ε_2	10	10.464	9.513	9.334	8.987
ε_3	5	4.310	3.231	4.434	4.014
q	0.5	0.545	0.517	0.459	0.538

is the absolute value.

4.1. 3-DOF Duffing nonlinear time-variant oscillator with fractional derivative elements

For the case of a 3-DOF Duffing nonlinear time-variant oscillator with fractional derivative terms, modeled as a standard chain-like system and using relative coordinates (e.g., [6]), Eq. (26) takes the form

$$\begin{bmatrix} M_1 & 0 & 0 \\ M_2 & M_2 & 0 \\ M_3 & M_3 & M_3 \end{bmatrix} \begin{bmatrix} \ddot{y}_1 \\ \ddot{y}_2 \\ \ddot{y}_3 \end{bmatrix} + \begin{bmatrix} C_1(t) & -C_2(t) & 0 \\ 0 & C_2(t) & -C_3(t) \\ 0 & 0 & C_3(t) \end{bmatrix} \begin{bmatrix} D^q[x_1] \\ D^q[x_2] \\ D^q[x_3] \end{bmatrix} +$$

$$\begin{bmatrix} K_1(t) & -K_2(t) & 0 \\ 0 & K_2(t) & -K_3(t) \\ 0 & 0 & K_3(t) \end{bmatrix} \begin{bmatrix} x_1 \\ x_2 \\ x_3 \end{bmatrix} + \begin{bmatrix} \varepsilon_1 K_1(t) x_1^3 \\ \varepsilon_2 K_2(t) x_2^3 \\ \varepsilon_3 K_3(t) x_3^3 \end{bmatrix} = \begin{bmatrix} f_1(t) \\ f_2(t) \\ f_3(t) \end{bmatrix}, \tag{38}$$

with $M_1 = M_2 = M_3 = 1$, and the time-varying damping and stiffness coefficients modeled as

$$\begin{aligned} C_1(t) &= 4 + 8\left(\frac{t}{T_0}\right)^2, \\ C_2(t) &= 2 + 4\left(\frac{t}{T_0}\right)^2, \\ C_3(t) &= 1 + 2\left(\frac{t}{T_0}\right)^2, \end{aligned} \tag{39}$$

$$\begin{aligned} K_1(t) &= 100 - 50\left(\frac{t}{T_0}\right)^2, \\ K_2(t) &= 50 - 25\left(\frac{t}{T_0}\right)^2, \\ K_2(t) &= 25 - 12.5\left(\frac{t}{T_0}\right)^2. \end{aligned} \tag{40}$$

The order of the fractional derivative is $q = 0.5$, while the nonlinearity parameters are $\varepsilon_1 = 15$, $\varepsilon_2 = 10$, and $\varepsilon_3 = 5$. The excitation is modeled as a non-stationary stochastic vector process with a non-separable EPS of

Table 1
Error estimates between the identified and the target parameter values considering various percentages of missing data.

Parameter	Complete		Missing(5%)/Noise		Missing(10%)/Noise		Missing(20%)/Noise	
	Error_1	Error_2	Error_1	Error_2	Error_1	Error_2	Error_1	Error_2
K_1	0.0350	0.0585	0.0094	0.1083	−0.0207	0.1020	−0.1617	0.1748
K_2	0.0719	0.0886	0.1415	0.1939	0.1252	0.2317	0.0707	0.1888
K_3	−0.0121	0.0686	0.0067	0.1717	−0.0339	0.1841	−0.0333	0.2543
C_1	−0.2332	0.2332	−0.2481	0.2481	0.0025	0.1572	−0.1536	0.2516
C_2	−0.1825	0.1825	−0.1189	0.1434	0.1834	0.3184	−0.1363	0.2937
C_3	−0.2390	0.2396	−0.1715	0.1999	0.1691	0.3940	−0.0118	0.3261

Table 3
Error estimates between the identified and the target values considering various percentages of missing data.

Parameter	Complete		Missing (5%)/Noise		Missing (10%)/Noise		Missing (20%)/Noise	
	$Error_1$	$Error_2$	$Error_1$	$Error_2$	$Error_1$	$Error_2$	$Error_1$	$Error_2$
ε_1	−0.0490	0.2164	−0.0499	0.3666	0.0412	0.3347	−0.1218	0.2916
ε_2	0.0464	0.2135	−0.1013	0.1630	−0.0666	0.1628	−0.0487	0.2737
ε_3	−0.1381	0.1381	−0.1972	0.6335	−0.1132	0.6160	−0.3475	0.3475
q	0.0903	0.2695	0.0768	0.3599	−0.0828	0.3430	0.0346	0.3206

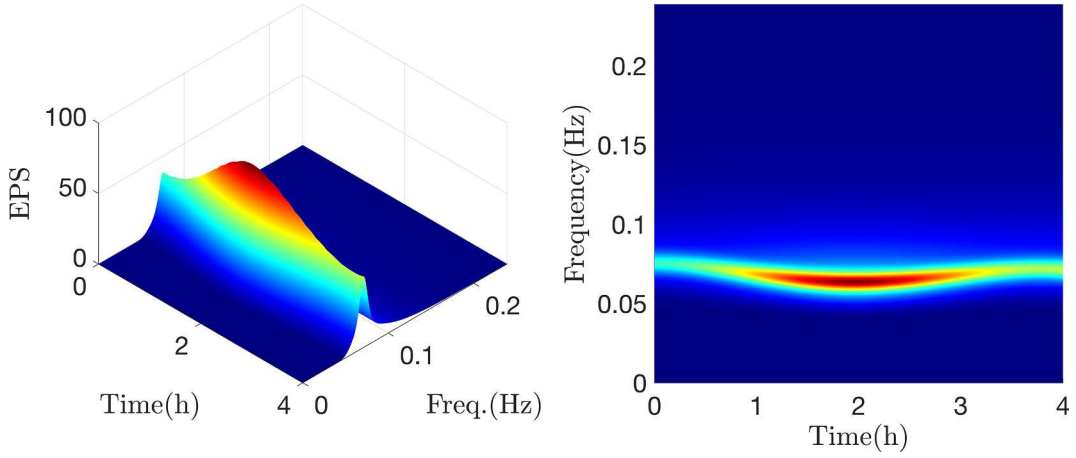

Fig. 14. Evolutionary JONSWAP power spectrum.

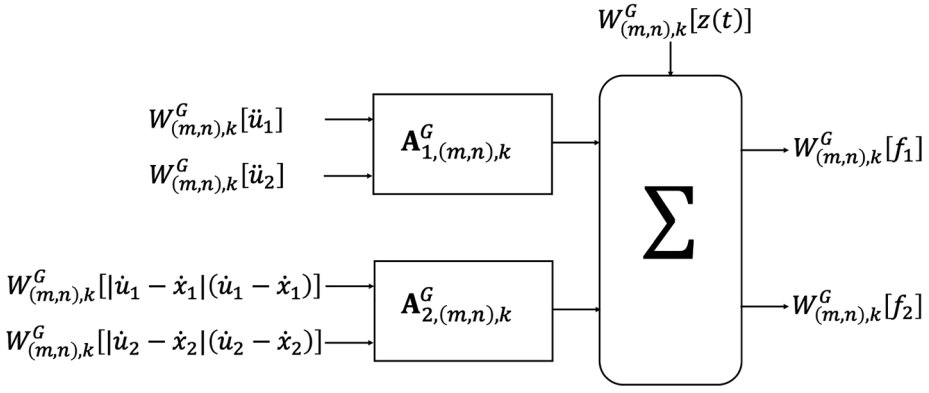

Fig. 15. 2-DOF system subjected to flow-induced forces recast as a MIMO problem.

the form

$$S_f\left(\omega, t\right) = S_0\left(\frac{\omega}{p_1}\right)^2 \exp(-bt)t^2 \exp\left(-\left(\frac{\omega}{p_2}\right)^2 t\right), \tag{41}$$

with the parameters values: $S_0 = 1$, $p_1 = 30\pi$, $p_2 = 10\pi$, $b = 0.15$. This excitation EPS, shown in Fig. 4, possesses some of the main characteristics observed in seismic motions, such as decreasing of the dominant frequency with time; see also [72].

Further, the corresponding MIMO model is shown in Fig. 5, with $\mathbf{x}_1 = \mathbf{x} = [x_1, x_2, x_3]^T$;$\mathbf{x}_2 = \mathbf{x}^3 = [x_1^3, x_2^3, x_3^2]^T$; and $\mathbf{f} = [f_1, f_2, f_3]^T$. Next, based on input-output records, the auto- and cross-EPS $S^{x_i x_l}_{(m,n),k}$, $S^{f_i f_l}_{(m,n),k}$, $S^{x_i x_j}_{(m,n),k}$, $S^{f_i f_j}_{(m,n),k}$, $S^{x_i f_j}_{(m,n),k}$ are determined, and the GHW-CCF $(\gamma^{f:x}_{(m,n),k})^2$ is estimated via Eq. (24). Indicatively, GHW-CCFs between the outputs and inputs considering the case of complete excitation-response time-histories and the case of both missing and corrupted data are shown in Figs. 6 and 7, respectively. Clearly, the estimated GHW-CCFs are useful in identifying time-varying frequency regions with high coherence values, where the identification technique is anticipated to exhibit better performance.

Next, considering Eq. (29) the GHW-FRFs $\mathbf{A}^G_{1,(m,n),k}$ of Eq. (30) and $\mathbf{A}^G_{i,(m,n),k}$, with $i = 2, ..., M+1$, related to $g(x, \dot{x})$ are determined. Indicatively, the elements $\mathbf{H}^G_{i,(m,n),k}(1, 1)$, $\mathbf{H}^G_{i,(m,n),k}(2, 2)$ and $\mathbf{H}^G_{i,(m,n),k}(3, 3)$ corresponding to the estimated GHW-FRF $\mathbf{A}^G_{1,(m,n),k}$ are plotted in Fig. 8, while Fig. 9 shows the same functions for an arbitrarily chosen time instant ($t = 6.2s$). In both figures, comparisons with the target GHW-FRFs are included as well, demonstrating a satisfactory degree of accuracy. In particular, it is seen that although the technique identifies correctly the positions of the natural frequencies, it tends to overestimate some of the corresponding GHW-FRF values.

The accuracy remains satisfactory even for the challenging case of both incomplete and corrupted data (40 dB noise), at least over the effective frequency domain where the three modes of vibration are prevalent. This is seen in Fig. 10 where the elements $\mathbf{H}^G_{i,(m,n),k}(1, 1)$, $\mathbf{H}^G_{i,(m,n),k}(2, 2)$ and $\mathbf{H}^G_{i,(m,n),k}(3, 3)$ corresponding to the estimated GHW-FRF $\mathbf{A}^G_{1,(m,n),k}$ (subject to 20% missing data) are plotted and compared with the target ones. In Fig. 11 the same functions are plotted for an indicative time instant $t = 6.2s$, however, various

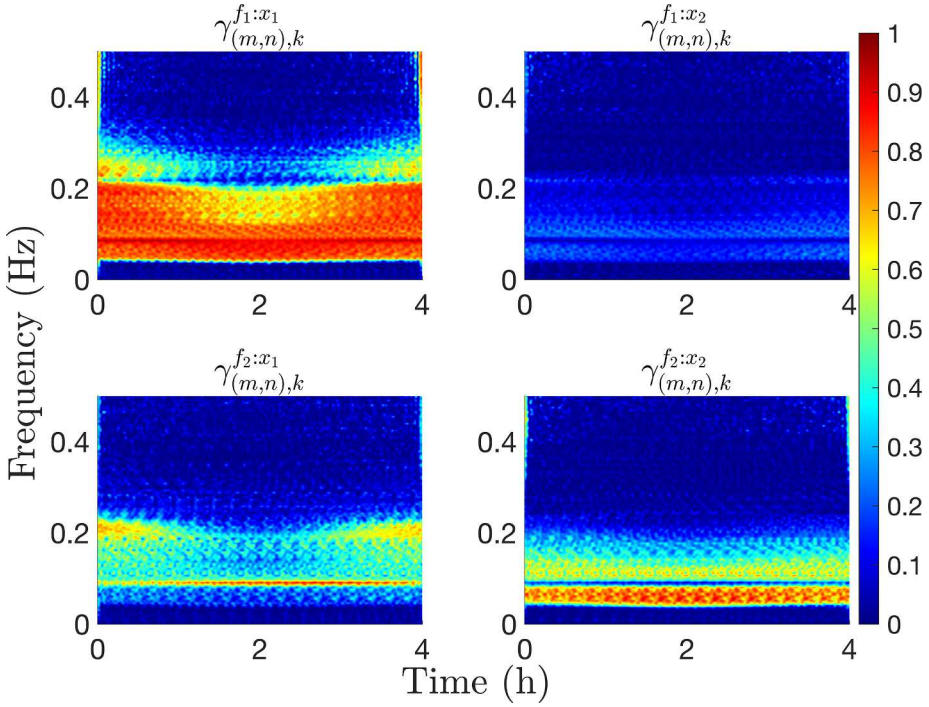

Fig. 16. Estimated GHW-CCF (complete time histories) for a 2-DOF system subject to flow-induced forces.

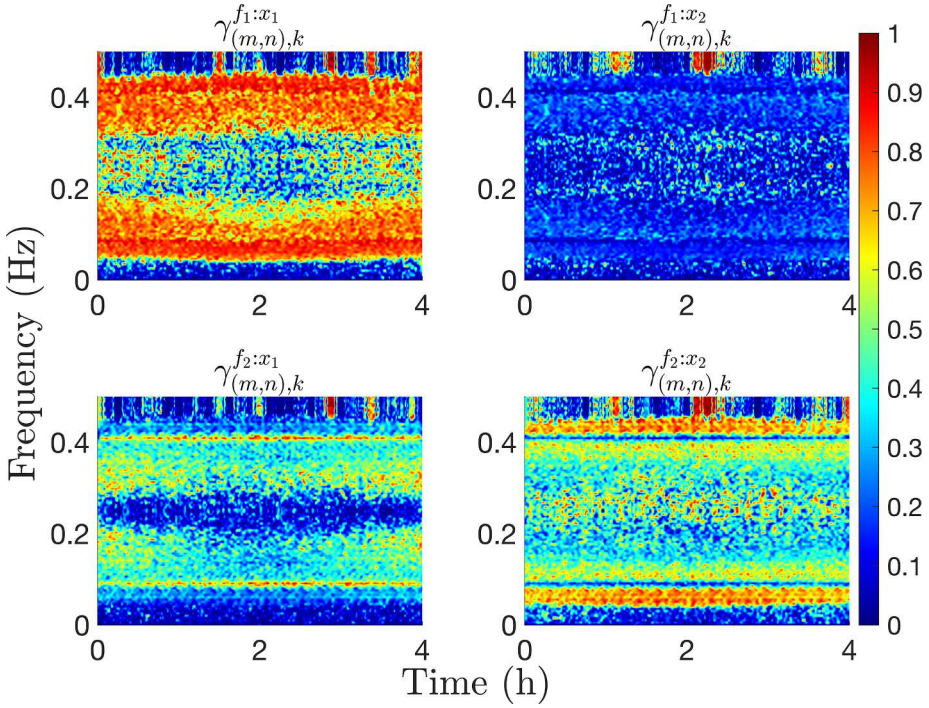

Fig. 17. Estimated GHW-CCF (incomplete time histories – 20% missing data – corrupted with noise) for a 2-DOF system subject to flow-induced forces.

percentages of missing data are considered, i.e., 5%, 10% and 20%. It appears that the degree of accuracy exhibited by the technique in identifying the position of the natural frequencies and the corresponding GHW-FRF values is, practically, not affected by the presence of incomplete data. In fact, missing data seem to impact mostly high-frequency regions, where the target GHW-FRF values are practically zero. Overall, it appears that the presence of incomplete and corrupted data does not compromise considerably the efficacy of the technique in determining the GHW-FRFs over the frequency region where the system is active. Next, following step 4 of Section 3.3, the time-dependent stiffness and damping parameters are identified and shown in Figs. 12 and 13, respectively, where the cases of complete and incomplete (20% missing data) time histories are demonstrated. It is seen that although notable discrepancies exist between the identified and the target parameters, the technique is capable of determining the salient features as well as the evolution in time of the system parameters in an average sense. As anticipated, the accuracy degree deteriorates in the presence of incomplete data and the oscillatory behavior of the estimates around the target values becomes more prevalent. However, the mean time-variant behavior of the system parameters is still estimated reasonably

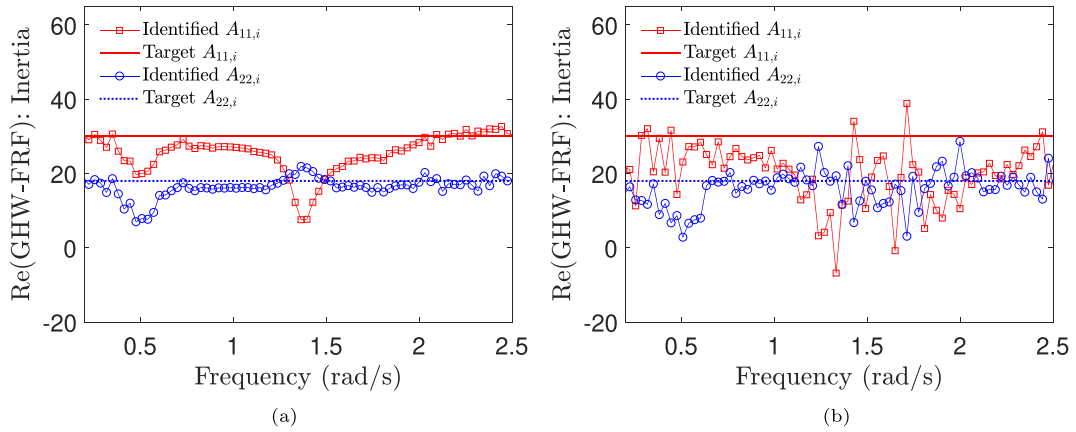

Fig. 18. Estimated GHW-FRF $\mathbf{A}^{G}_{1,(m,n),k}$ at $t = 50s$ for a 2-DOF system subject to flow-induced forces; (a) Complete time histories; (b) Incomplete time histories corrupted with noise (20% missing data).

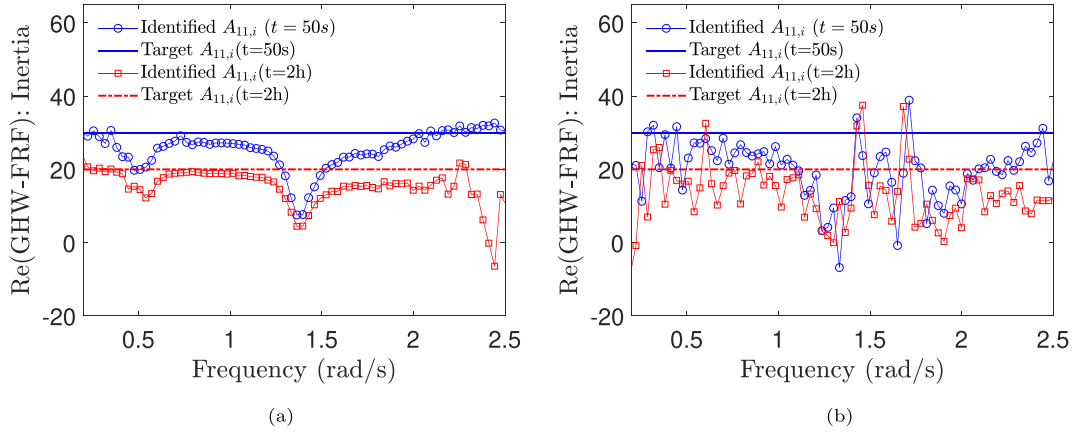

Fig. 19. GHW-TF $\mathbf{A}^{G}_{1,(m,n),k}$ component (1, 1) at various time instants corresponding to the inertia coefficient; (a) Complete time histories; (b) Incomplete time histories corrupted with noise (20% missing data).

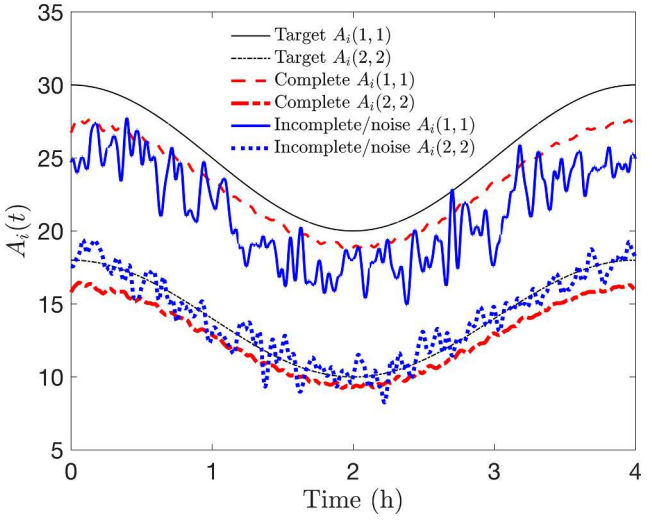

Fig. 20. Comparison between the target and the estimated inertia coefficient matrix elements for a 2-DOF system subject to flow-induced forces.

well.

The aforementioned remarks are further corroborated by the results shown in Table 1, where Error_1 and Error_2 are calculated for various percentages of missing data (5%, 10% and 20%). Clearly, Error_1 definition serves to quantify the average error in time, while neglecting localized oscillatory deviations from the target values. On the other hand, Error_2 definition can be construed as "stricter" since it accounts for all deviations from the target. In this regard, overall smaller Error_1 values than Error_2 are observed in Table 1, indicating that the estimated parameters tend to oscillate around the target ones and succeed in capturing the average in time system behavior. Also, it is worth noting that Error_2 values, in general, tend to decrease for smaller amounts of missing data, indicating that the magnitude of oscillations reduces as the number of missing data becomes smaller.

Further, the identified fractional derivative order and nonlinear function parameters are shown in Table 2, and error estimates between the identified and the target values considering various percentages of missing data are shown in Table 3. In particular, for the identification of the constant q, ε_1, ε_2, and ε_3 values, the respective averages over time estimates are considered. Note that once the stiffness elements ($K_{i,k}$) are identified, the nolinearity parameters ε_i can be determined as $\varepsilon_i = \frac{\mathrm{A}^{G}_{2,(m,n),k}\left(i,i\right)}{K_{i,k}}$, for i = 1, 2, 3. In a similar manner as in Table 1, it is seen that Error_1 values are in general smaller than Error_2 values.

4.2. 2-DOF nonlinear time-variant offshore structural system subject to flow-induced forces

In this example, an offshore structural system subject to flow-induced forces is considered. The Morison model is adopted, which utilizes an inertial term accounting for the influence of the fluid mass around the submerged structure, and a drag-type nonlinearity accounting for the relative velocity between the structure and the fluid

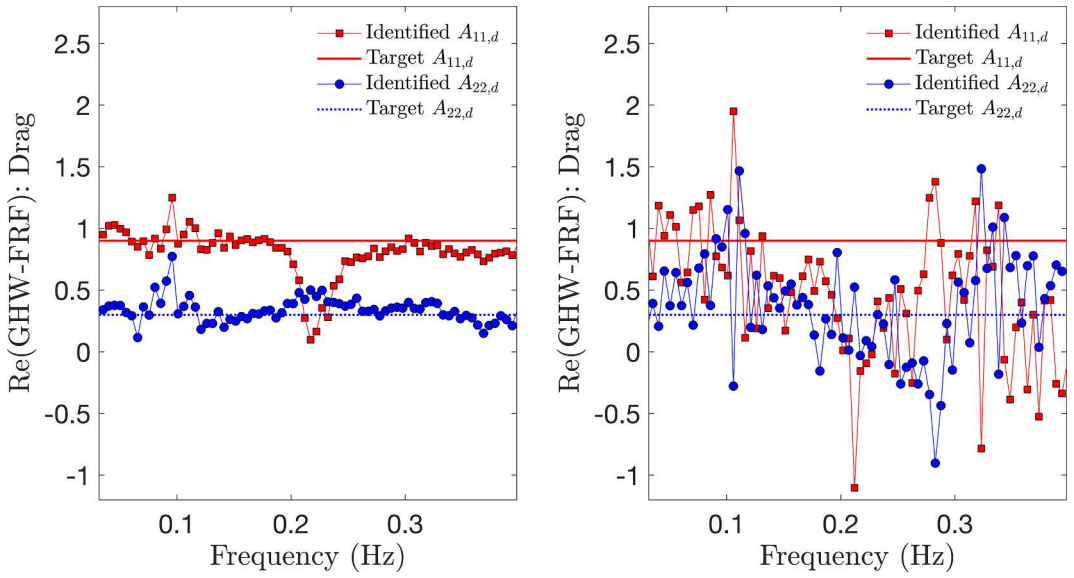

Fig. 21. Estimated GHW-FRF $\mathbf{A}^{G}_{2,(m,n),k}$ at $t = 50s$ for a 2-DOF system subject to flow-induced forces; (a) Complete time histories; (b) Incomplete time histories corrupted with noise (20% missing data).

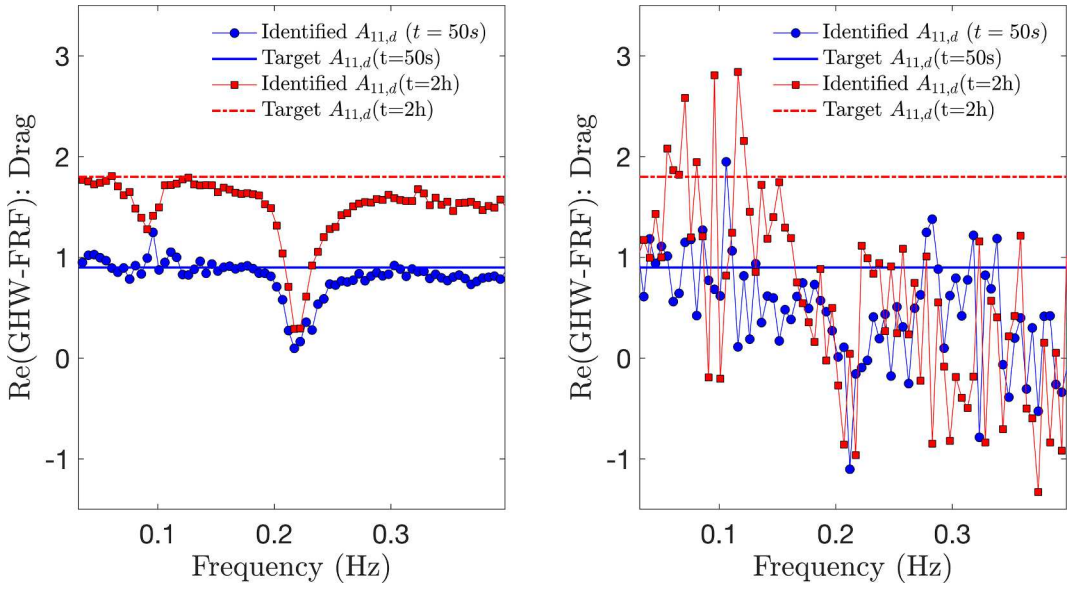

Fig. 22. GHW-TF $\mathbf{A}^{G}_{2,(m,n),k}$ component (1, 1) at various time instants corresponding to the drag coefficient; (a) Complete time histories; (b) Incomplete time histories corrupted with noise (20% missing data).

particles (e.g., [10]). For practical applications, the inertia and drag coefficients are to be determined experimentally and depend on a number of factors, such as the structure geometry, Reynolds number, surface roughness and the Iversen's modulus. It is noted, however, that although in reality these coefficients are both time- and space-dependent (e.g., [73–75]), most research efforts involving Morison type modeling consider them as constants (e.g., [11]). In the present example, and to address partly the above inconsistency, the coefficients to be identified are modeled as time-dependent functions.

Further, it is common practice in marine engineering to model the sea state as a stationary random process. In this regard, classical models such as the Pierson-Moskowitz [76] and the JONSWAP [77] power spectra are typically employed to define a stationary free-surface elevation for a fully developed sea. Herein, an evolutionary version of the JONSWAP spectrum, originally proposed in [31], is adopted to account for time-dependent sea states. This JONSWAP EPS, shown in Fig. 14, is given by the expression

$$S_h(\omega, t) = F(t) g^2 \omega^{-5} \exp\left[-1.25\left(\frac{\omega_p(t)}{\omega}\right)^4\right] \times \exp\left\{\ln(\gamma)\exp\left[-\frac{(\omega-\omega_p(t))^2}{2\chi^2\omega_p^2(t)}\right]\right\}, \tag{42}$$

where

$$F(t) = \frac{H_s^2(t)}{16}\left\{\int_0^\infty g^2\omega^{-5}\exp\left[-1.25\left(\frac{\omega_p(t)}{\omega}\right)^4\right]\exp\left\{\ln(\gamma)\exp\left[-\frac{(\omega-\omega_p(t))^2}{2\chi^2\omega_p^2(t)}\right]\right\}d\omega\right\}^{-1}, \tag{43}$$

and

$$\omega_p(t) = 0.2353\left(\frac{H_s(t)}{4g}\right)^{-\frac{1}{2}}. \tag{44}$$

In Eqs. (42)–(44) g is the gravitational acceleration, $\chi = 0.08$, $\gamma = 3.3$,

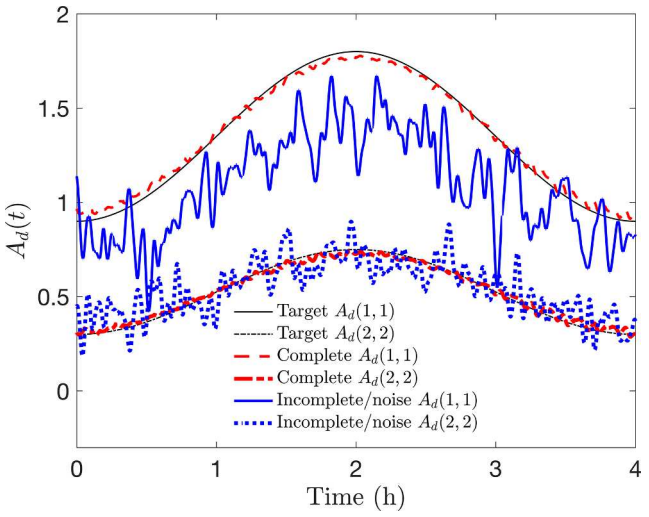

Fig. 23. Comparison between the target and the estimated drag coefficient matrix elements for a 2-DOF system subject to flow-induced forces.

Table 4
Error estimates between the identified and the target parameter values

Parameter	Complete		Missing (20%)/Noise	
	Error_1	Error_2	Error_1	Error_2
$A_i(1,1)$	0.069202	-0.069202	0.148162	−0.148146
$A_i(2,2)$	0.083397	-0.083397	0.047642	0.002323
$A_d(1,1)$	0.020972	0.009931	0.193157	−0.185505
$A_d(2,2)$	0.030817	0.008805	0.161001	0.062988

and $H_s(t)$ is estimated based on buoy data recorded at the western Gulf of Alaska; see [31] for more details. In passing, it is noted that the flow velocity $\dot{\mathbf{u}}$ can be estimated from the sea elevation by employing the linear wave theory [78].

Next, following [63], the governing equation of a 2-DOF system subject to flow-induced forces takes the form

$$\begin{bmatrix} M_1 & 0 \\ 0 & M_2 \end{bmatrix}\begin{bmatrix} \ddot{x}_1 \\ \ddot{x}_2 \end{bmatrix} + \begin{bmatrix} C_1+C_2 & -C_2 \\ -C_2 & C_2 \end{bmatrix}\begin{bmatrix} \dot{x}_1 \\ \dot{x}_2 \end{bmatrix} + \begin{bmatrix} K_1+K_2 & -K_2 \\ -K_2 & K_2 \end{bmatrix}\begin{bmatrix} x_1 \\ x_2 \end{bmatrix} = \begin{bmatrix} A_{1d}(t) & A_{2d}(t) \\ A_{2d}(t) & A_{1d}(t) \end{bmatrix}\begin{bmatrix} |\dot{u}_1-\dot{x}_1|(\dot{u}_1-\dot{x}_1) \\ |\dot{u}_2-\dot{x}_2|(\dot{u}_2-\dot{x}_2) \end{bmatrix} + \begin{bmatrix} A_{1i}(t) & A_{2i}(t) \\ A_{2i}(t) & A_{1i}(t) \end{bmatrix}\begin{bmatrix} \ddot{u}_1 \\ \ddot{u}_2 \end{bmatrix}, \tag{45}$$

where $M_1 = M_2 = 50$, $C_1 = 2$, $C_2 = 3$, $K_1 = 50$, and $K_2 = 30$. The water particle velocities $\dot{\mathbf{u}}_1$ and $\dot{\mathbf{u}}_2$ are generated simultaneously at depths 10 and 15 m from a single random wave with steady currents of 1.5 m/s and 1 m/s being added, respectively. In this example, the time-variant drag coefficients $A_{1i}(t)$ and $A_{2i}(t)$, and the time-variant inertia coefficients $A_{1d}(t)$ and $A_{2d}(t)$ are designated as the unknowns to be identified. In this regard, smoothly varying with time generic functions (of a sinusoidal form) are adopted to describe the behavior of the coefficients based on the analysis and experimental data presented in [74,75]. Next, applying the herein developed identification technique, the corresponding MIMO model takes the form (see also Fig. 15)

$$\mathbf{A}_i\mathbf{x}_1 + \mathbf{A}_d\mathbf{x}_2 = \mathbf{f}, \tag{46}$$

where $\mathbf{x}_1 = \ddot{\mathbf{u}} = [\ddot{u}_1, \ddot{u}_2]^T$; $\mathbf{x}_2 = |\dot{\mathbf{u}} - \dot{\mathbf{x}}|(\dot{\mathbf{u}} - \dot{\mathbf{x}}) = [|\dot{u}_1 - \dot{x}_1|(\dot{u}_1 - \dot{x}_1), |\dot{u}_2 - \dot{x}_2|(\dot{u}_2 - \dot{x}_2)]^T$; $\mathbf{f} = \mathbf{M}\ddot{\mathbf{x}} + \mathbf{C}\dot{\mathbf{x}} + \mathbf{K}\mathbf{x}$, and the time-variant matrices $\mathbf{A_i}$ and $\mathbf{A_d}$ to be identified are given by

$$\mathbf{A_i} = \begin{bmatrix} A_{1i}(t) & A_{2i}(t) \\ A_{2i}(t) & A_{1i}(t) \end{bmatrix}, \quad \mathbf{A_d} = \begin{bmatrix} A_{1d}(t) & A_{2d}(t) \\ A_{2d}(t) & A_{1d}(t) \end{bmatrix}. \tag{47}$$

As mentioned in Section 3.1, the designation of the inputs and outputs in the MISO identification technique can be rather arbitrary, and such definitions can change depending on which parameters are unknown. This is seen in Eq. (46) where the relevant terms have been re-arranged accordingly.

Following the evaluation of the auto- and cross-EPS $S^{x_ix_i}_{(m,n),k}$, $S^{f_if_i}_{(m,n),k}$, $S^{x_ix_j}_{(m,n),k}$, $S^{f_if_j}_{(m,n),k}$, $S^{x_if_j}_{(m,n),k}$, the GHW-CCF $(\gamma^{f:x}_{(m,n),k})^2$ is estimated via Eq. (25) and shown for various time instants in Figs. 16,17 for the cases of complete and of incomplete and corrupted data, respectively.

Next, the GHW-FRFs corresponding to the time-dependent coefficient matrices $\mathbf{A}^G_{1,(m,n),k}$ and $\mathbf{A}^G_{2,(m,n),k}$ are determined. In Fig. 18, the estimated $\mathbf{A}^G_{1,(m,n),k}$ components are plotted for a given time instant, while in Fig. 19 the estimates for component (1, 1) of $\mathbf{A}^G_{1,(m,n),k}$ are shown for two arbitrary time instants. Note that based on the definition of the inertia and drag coefficients, these are equal to the real parts of the respective GHW-FRFs. Clearly, the accuracy degree of the estimated $\mathbf{A}^G_{1,(m,n),k}$ varies across the joint time-frequency domain, and therefore, the information provided by the GHW-CCF (see Figs. 16,17) in selecting appropriate time-frequency regions is catalytic in the ensuing analysis. In this regard, the identified inertia coefficients are plotted and compared with the target ones in Fig. 20. It is seen that the technique succeeds in capturing satisfactorily the salient features of the time-dependent behavior of the parameters. In a similar manner as in Example 4.1, the accuracy degree deteriorates when incomplete and corrupted data are considered, however, the performance of the technique remains satisfactory. Similar results are shown in Figs. 21–23 corresponding to the GHW-FRF $\mathbf{A}^G_{2,(m,n),k}$. Specifically, in Fig. 21 the estimated $\mathbf{A}^G_{2,(m,n),k}$ components are plotted for a given time instant, while in Fig. 22 the estimates for component (1, 1) of $\mathbf{A}^G_{2,(m,n),k}$ are shown for two arbitrary time instants. It is worth noting that despite the relatively poor GHW-FRF estimates in the presence of incomplete and corrupted data, utilizing frequency intervals corresponding to relatively high coherence values yields satisfactory estimates for the time-dependent drag coefficients in Fig. 23. The above remarks are further corroborated by relevant error estimates in Table 4, where it is seen that the drag coefficients estimates appear more sensitive and the related errors increase significantly in the presence of missing data compared to the inertia coefficients estimates.

This behavior can be explained by the presence of the term $\dot{\mathbf{x}} = [\dot{x}_1, \ \dot{x}_2]$ in the nonlinear functional multiplying the drag coefficients in Eq. (45). Specifically, the system response velocity $\dot{\mathbf{x}}$ tends to exhibit a wider spectral band than $\ddot{\mathbf{u}}$; thus, affecting negatively the performance of compressive sampling in recovering the missing information.

5. Concluding remarks

Various system identification techniques exist in the literature that can handle non-stationary measured time-histories, or cases of incomplete data, or address systems following a fractional calculus modeling. However, there are not many (if any) techniques that can address all three aforementioned challenges simultaneously in a consistent manner. In this paper, the MISO identification technique proposed in [28], and generalized in [36,27] for addressing incomplete non-stationary data and fractional derivative modeling, has been extended herein to account for MDOF systems. Specifically, the technique relies on recasting the governing equation as a set of MIMO systems in the wavelet domain. Next, an l_1-norm minimization procedure based on compressive sampling theory has been employed for determining the wavelet coefficients of the available incomplete non-stationary input-output data. Finally, these wavelet coefficients have been utilized to reconstruct the non-stationary incomplete signals, and consequently, to determine system related time- and frequency-dependent wavelet-based frequency response functions and associated parameters. Two

illustrative MDOF systems have been considered in the numerical examples for demonstrating the reliability of technique. The first refers to a nonlinear time-variant system with fractional derivative terms, while the second addresses a nonlinear offshore structural system subjected to flow-induced forces. It is worth noting that for the offshore system, a novel recently proposed evolutionary version of the widely used JONSWAP spectrum has been employed for modeling the non-stationary free-surface elevation in cases of time-dependent sea states. It has been shown that even in cases where the technique fails to capture the details of the time-varying behavior, it still succeeds in identifying the time-varying trend of the system parameters in an average sense.

Acknowledgements

I. A. Kougioumtzoglou gratefully acknowledges the support by the CMMI Division of the National Science Foundation, USA (Award number: 1724930). K. R. M. dos Santos gratefully acknowledges the support by the Brazilian Federal Agency for Coordination of Improvement of Higher Education Personnel (CAPES) (Award number: BEX/13406-13-2).

References

[1] Giannakis G, Serpedin E. A bibliography on nonlinear system identification. Signal Process 2001;81(3):533–80.
[2] Kerschen G, Worden K, Vakakis A, Golinval J-C. Past, present and future of nonlinear system identification in structural dynamics. Mech Syst Signal Process 2006;20(3):505–92.
[3] Reynders E. System identification methods for (operational) modal analysis: review and comparison. Arch Comput Methods Eng 2012;19:51–124.
[4] Billings SA. Nonlinear system identification. John Wiley & Sons; 2013.
[5] Adeniran AA, Ferik SE. Modeling and identification of nonlinear systems: a review of the multimodel approach part 1. IEEE Trans Syst, Man, Cybern: Syst 2017;47(7):1149–59.
[6] Roberts JB, Spanos PD. Random vibration and statistical linearization. Courier Corporation; 2003.
[7] Wen Y. Methods of random vibration for inelastic structures. Appl Mech Rev 1989;42(2):39–52.
[8] Bertotti G, Mayergoyz ID. The science of hysteresis: Hysteresis in materials. Gulf Professional Publishing; 2006.
[9] Ikhouane F, Rodellar J. Systems with hysteresis: analysis, identification and control using the Bouc-Wen model. John Wiley & Sons; 2007.
[10] Morison J, Johnson J, Schaaf S. The force exerted by surface waves on piles. J Petrol Technol 1950;2(05):149–54.
[11] Spanos P, Ghosh R, Finn L, Halkyard J. Coupled analysis of a spar structure: Monte Carlo and statistical linearization solutions. J Offshore Mech Arctic Eng 2005;127(1):11–6.
[12] Psaros AF, Brudastova O, Malara G, Kougioumtzoglou IA. Wiener path integral based response determination of nonlinear systems subject to non-white, non-gaussian, and non-stationary stochastic excitation. J Sound Vib 2018;433:314–33.
[13] Di Paola M, Pirrotta A, Valenza A. Visco-elastic behavior through fractional calculus: an easier method for best fitting experimental results. Mech Mater 2011;43(12):799–806.
[14] Di Paola M, Failla G, Pirrotta A, Sofi A, Zingales M. The mechanically based non-local elasticity: an overview of main results and future challenges. Philos Trans R Soc A: Math Phys Eng Sci 2013;371(1993):20120433.
[15] Tarasov VE. Fractional mechanics of elastic solids: continuum aspects. J Eng Mech 2016;143(5):D4016001.
[16] Mallat S, A Wavelet Tour of Signal Processing, 3rd ed.; 2009.
[17] Wang Y, Li J, Stoica P. Spectral analysis of signals: the missing data case. Morgan & Claypool; 2006.
[18] Rossikhin YA, Shitikova MV. Application of fractional calculus for dynamic problems of solid mechanics: novel trends and recent results. Appl Mech Rev 2010;63(010801):1–52.
[19] Kijewski T, Kareem A. Wavelet transforms for system identification in civil engineering. Comput-Aided Civil Infrastruct Eng 2003;18:339–55.
[20] Spanos P, Failla G. Wavelets: theoretical concepts and vibrations related applications. Sage 2005.
[21] Yang Y, Nagarajaiah S. Harnessing data structure for recovery of randomly missing structural vibration responses time history: Sparse representation versus low-rank structure. Mech Syst Signal Process 2016;74:165–82 Special Issue in Honor of Professor Simon Braun.
[22] Huang Y, Beck JL, Wu S, Li H. Bayesian compressive sensing for approximately sparse signals and application to structural health monitoring signals for data loss recovery. Prob Eng Mech 2016;46:62–79.
[23] Deng R, Davies P, Bajaj A. Flexible polyurethane foam modelling and identification of viscoelastic parameters for automotive seating applications. J Sound Vib 2003;262(3):391–417.
[24] Tang Y, Liu H, Wang W, Lian Q, Guan X. Parameter identification of fractional order systems using block pulse functions. Signal Process 2015;107:272–81.
[25] Zou Y, Li S, Shao B, Wang B. State-space model with non-integer order derivatives for lithium-ion battery. Appl Energy 2016;161:330–6.
[26] Di Matteo A, Di Paola M, Pirrotta A. Innovative modeling of tuned liquid column damper controlled structures. Smart Struct Syst 2016;18:117–38.
[27] Kougioumtzoglou IA, dos Santos KRM, Comerford L. Incomplete data based parameter identification of nonlinear and time-variant oscillators with fractional derivative elements. Mech Syst Signal Proc 2017;94:279–96.
[28] Bendat JS, Palo PA, Coppolino RN. A general identification technique for nonlinear differential equations of motion. Prob Eng Mech 1992;7:43–61.
[29] Bendat JS, Coppolino RN, Palo PA. Identification of physical parameters with memory in non-linear systems. Int J Non-Linear Mech 1995;30(6):841–60.
[30] Bendat JS. Nonlinear systems techniques and applications. John Wiley & Sons; 1998.
[31] Spanos PD, Laface V, Malara G, Arena F. Simulation of non-stationary sea waves compatible with storm data. Computational Stochastic Mechanics – Proceedings of the 8th International Conference (CSM-8). 2018. ISBN 978-981-11-2723-6.
[32] Newland DE. Harmonic and musical wavelets. Proc R Soc A 1994;444(1922):605–20.
[33] Spanos PD, Kong F, Li J, Kougioumtzoglou IA. Harmonic wavelets based excitation response relationships for linear systems: a critical perspective. Prob Eng Mech 2016;44:163–73.
[34] Spanos PD, Kougioumtzoglou IA. Harmonic wavelets based statistical linearization for response evolutionary power spectrum determination. Prob Eng Mech 2012;27(1):57–68.
[35] Kougioumtzoglou IA, Spanos P. Harmonic wavelets based response evolutionary power spectrum determination of linear and non-linear oscillators with fractional derivative elements. Int J Non-Linear Mech 2016;80:66–75.
[36] Kougioumtzoglou IA, Spanos PD. An identification approach for linear and non-linear time-variant structural systems via harmonic wavelets. Mech Syst Signal Proc 2013;37:338–52.
[37] Nason GP, von Sachs R, Kroisandt G. Wavelet processes and adaptive estimation of the evolutionary wavelet spectrum. J R Stat Soci Ser B (Stat Methodol) 2000;62(2):271–92.
[38] Spanos PD, Tezcan J, Tratskas P. Stochastic processes evolutionary spectrum estimation via harmonic wavelets. Comput Methods Appl Mech Eng 2005;194(12–16):1367–83.
[39] Kougioumtzoglou IA, Kong F, Spanos PD, Li J, Some observations on wavelets based evolutionary power spectrum estimation, Proceedings of the Stochastic Mechanics Conference (SM12), Ustica, Italy, 7–10 June, 2012, Meccanica dei Materiali e delle Strutture 3 (2012) 37–44.
[40] Candes EJ, Romberg JK, Tao T. Robust uncertainty principles: exact signal reconstruction from highly incomplete frequency information. Trans Inf Theory 2006;52:489–509.
[41] Candes EJ, Romberg JK, Tao T. Stable signal recovery from incomplete and inaccurate measurements. Commun Pure Appl Math 2006;59:1207–23.
[42] Candes EJ. The restricted isometry property and its implications for compressed sensing. CR Math 2008;346(9):589–92.
[43] Eldar YC, Kutyniok G. Compressed sensing: theory and applications. Cambridge University Press; 2012.
[44] Chen SS, Donoho DL, Saunders MA. Atomic decomposition by basis pursuit. J Sci Comput 1998;20:33–61.
[45] Tropp JA, Gilbert AC. Signal recovery from random measurements via orthogonal matching pursuit. Trans Inf Theory 2007;53:4655–66.
[46] Boche H, Compressed Sensing and Its Applications: MATHEON Workshop 2013, Birkhäuser; 2015.
[47] Boche H, Compressed Sensing and Its Applications: Second MATHEON Workshop 2015, Birkhäuser; 2017.
[48] Boche H, Compressed Sensing and Its Applications: Third International MATHEON Workshop 2017, Birkhäuser; 2019.
[49] Klis R, Chatzi EN. Vibration monitoring via spectro-temporal compressive sensing for wireless sensor networks. Struct Infrastruct 2017;13:195–209.
[50] Gkoktsi K, Giaralis A. Assessment of sub-Nyquist deterministic and random data sampling techniques for operational modal analysis. Struct Health Monit 2017;16(5):630–46.
[51] Jayawardhana M, Zhu X, Liyanapathirana R. Compressive sensing for efficient health monitoring and effective damage detection of structures. Mech Syst Signal Proc 2017;84:414–30.
[52] Yang Y, Nagarajaiah S. Robust data transmission and recovery of images by compressed sensing for structural health diagnosis. Struct Control Health Monit 2017;24:1856.
[53] Yao R, Pakzad SN, Venkitasubramaniam P. Compressive sensing based structural damage detection and localization using theoretical and metaheuristic statistics. Struct Control Health Monit 2017;24:1881.
[54] Ji S, Tan C, Yang P, Sun Y-J, Fu D, Wang J. Compressive sampling and data fusion-based structural damage monitoring in wireless sensor network. J Supercomput 2018;74:1108–31.
[55] Bao Y, Shi Z, Wang X, Li H. Compressive sensing of wireless sensors based on group sparse optimization for structural health monitoring. Struct Health Monitor 2018;17(4):823–36.
[56] Comerford L, Kougioumtzoglou IA, Beer M. Compressive sensing based stochastic process power spectrum estimation subject to missing data. Prob Eng Mech 2016;44:66–76.
[57] Zhang Y, Comerford L, Kougioumtzoglou IA, Beer M. L_p-norm minimization for stochastic process power spectrum estimation subject to incomplete data. Mech Syst Signal Proc 2018;101:361–76.

[58] Laface V, Kougioumtzoglou IA, Malara G, Arena F. Efficient processing of water wave records via compressive sensing and joint time-frequency analysis via harmonic wavelets. Appl Ocean Res 2017;69:1–9.
[59] Malara G, Kougioumtzoglou IA, Arena F. Extrapolation of random wave field data via compressive sampling. Ocean Eng 2018;157:87–95.
[60] Oldham KB, Spanier J. The fractional calculus: theory and applications of differentiation and integration to arbitrary order. Dover Publications; 2006.
[61] Selvam RP, Bhattacharyya SK. System identification of a coupled two DOF moored floating body in random ocean waves. J Offshore Mech Arctic Eng 2006;128:191–202.
[62] Raman S, Yim SCS, Palo PA. Nonlinear model for sub- and superharmonic motions of a MDOF moored structure, Part 1 – system identification. J Offshore Mech Arctic Eng 2005;127:283–90.
[63] Spanos PD, Lu R. Nonlinear system identification in offshore structural reliability. J Offshore Mech Arctic Eng 1995;117:171–7.
[64] Perreault EJ, Kirsch RF, Acosta AM. Multiple-input, multiple-output system identification for characterization of limb stiffness dynamics. Biol Cybern 1999;80:327–37.
[65] Bendat JS, Piersol AG, Data Random. Analysis and measurement procedures. 2nd ed. John Wiley & Sons; 1986.
[66] Rice HJ, Fitzpatrick JA. A generalized technique for spectral analysis of non-linear systems. Mech Syst Signal Proc 1988;2:195–207.
[67] Bendat JS, Piersol AG. Engineering applications of correlation and spectral analysis. 2nd ed. John Wiley & Sons; 1993.
[68] Zeldin BA, Spanos PD. Spectral identification of nonlinear structural systems. J Eng Mech 1998;124:728–33.
[69] Shinozuka M, Deodatis G. Simulation of multi-dimensional gaussian stochastic fields by spectral representation. Appl Mech Rev 1996;49(1):29–53.
[70] Liang J, Chaudhuri SR, Shinozuka M. Simulation of nonstationary stochastic processes by spectral representation. J Eng Mech 2007;133(6):616–27.
[71] Koh CG, Kelly JM. Application of fractional derivatives to seismic analysis of base-isolated models. Earthq Eng Struct Dyn 1990;19:229–41.
[72] Tubaldi E, Kougioumtzoglou IA. Nonstationary stochastic response of structural systems equipped with nonlinear viscous dampers under seismic excitation. Earthq Eng Struct Dyn 2015;44:121–38.
[73] Fish P, Dean R, Heaf N. Fluid-structure interaction in morison's equation for the design of offshore structures. Eng Struct 1980;2(1):15–26.
[74] Jordan SK, Fromm JE. Oscillatory drag, lift, and torque on a circular cylinder in a uniform flow. Phys Fluids 1972;15(3):371–6.
[75] Chapter 12 – calculation of wave forces on three-dimensional space frames, in: P. Boccotti (Ed.), Wave Mechanics and Wave Loads on Marine Structures, Butterworth-Heinemann, Oxford, 2015, pp. 227 – 243.
[76] Pierson JW, Moskowitz L. A proposed spectral form for fully developed wind seas based on the similarity theory of s. a. kitaigorodskii. J Geophys Res 1964;69(24):5181–90.
[77] Hasselmann K, Barnett T, Bouws E, Carlson H, Cartwright D, Enke K, et al. Measurements of wind-wave growth and swell decay during the joint north sea wave project (jonswap). Ergnzungsheft zur Deutschen Hydrographischen Zeitschrift Reihe A 1973;8(12):1–95.
[78] Donelan M, Anctil F, Doering J. A simple method for calculating the velocity field beneath irregular waves. Coast Eng 1992;16(4):399–424.